

# Iron-rich Fe–O compounds at Earth's core pressures

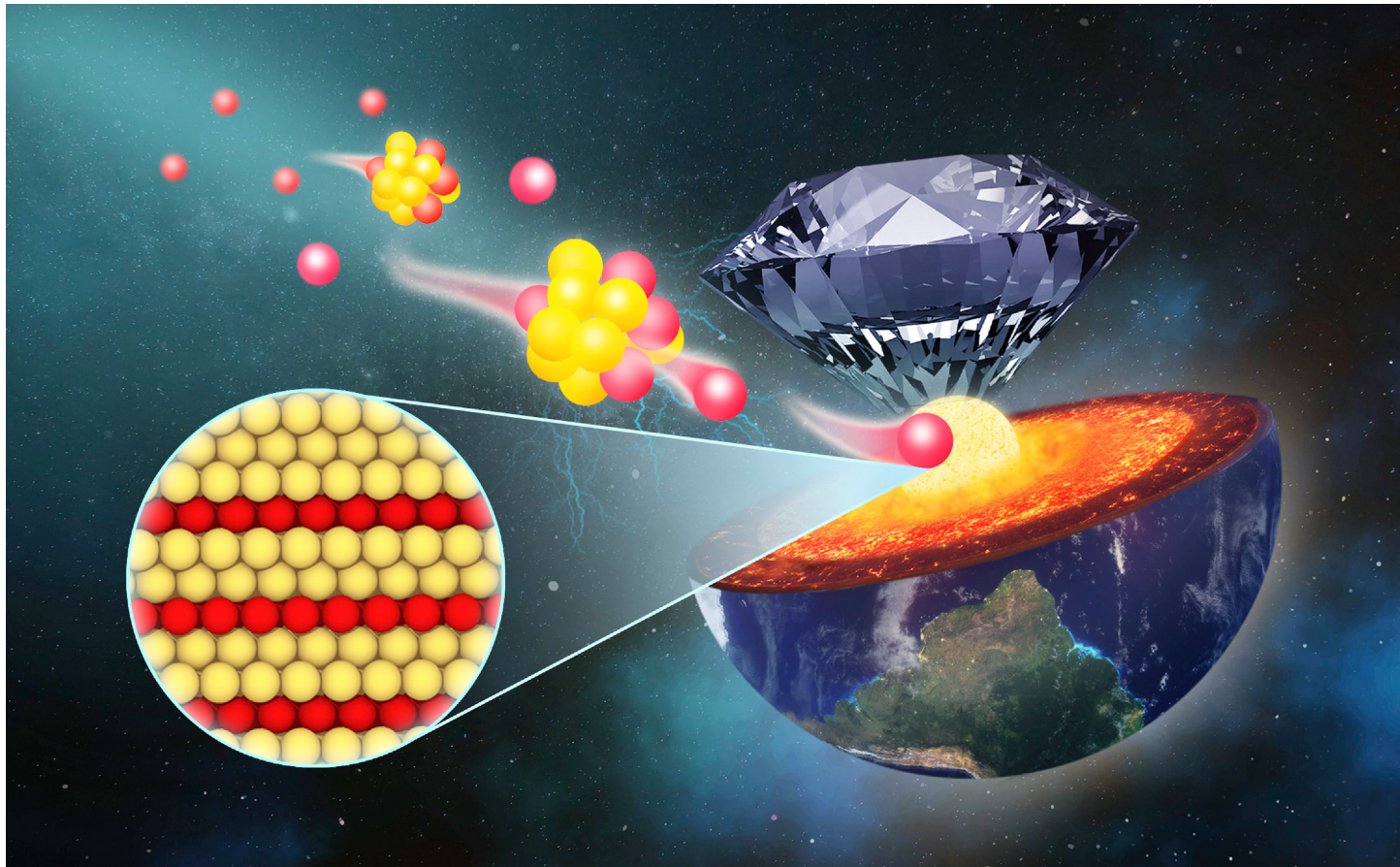
Jin Liu,<sup>1,2,9,\*</sup> Yang Sun,<sup>3,9</sup> Chaojia Lv,<sup>1</sup> Feng Zhang,<sup>4</sup> Suyu Fu,<sup>5</sup> Vitali B. Prakapenka,<sup>6</sup> Caizhuang Wang,<sup>4</sup> Kaiming Ho,<sup>4</sup> Jungfu Lin,<sup>5,\*</sup> and Renata M. Wentzcovitch<sup>3,7,8,\*</sup>

\*Correspondence: jin.liu@hpstar.ac.cn (J.L.); afu@jsg.utexas.edu (J.L.); rmw2150@columbia.edu (R.M.W.)

Received: July 22, 2022; Accepted: November 13, 2022; Published Online: November 15, 2022; <https://doi.org/10.1016/j.xinn.2022.100354>

© 2022 The Authors. This is an open access article under the CC BY-NC-ND license (<http://creativecommons.org/licenses/by-nc-nd/4.0/>).

## GRAPHICAL ABSTRACT



## PUBLIC SUMMARY

- A family of Fe-rich  $\text{Fe}_n\text{O}$  compounds is revealed under Earth's core conditions
- The  $\text{Fe}_n\text{O}$  compounds feature close-packed Fe and O monolayers
- The separate O monolayer stabilizes  $\text{Fe}_n\text{O}$  compounds at multi-megabar pressures
- The Earth's inner core can contain more oxygen than expected due to  $\text{Fe}_n\text{O}$  phases
- It alters our understanding of thermal evolution and seismic features of the core



# Iron-rich Fe–O compounds at Earth's core pressures

Jin Liu,<sup>1,2,9,\*</sup> Yang Sun,<sup>3,9</sup> Chaojia Lv,<sup>1</sup> Feng Zhang,<sup>4</sup> Suyu Fu,<sup>5</sup> Vitali B. Prakapenka,<sup>6</sup> Caizhuang Wang,<sup>4</sup> Kaiming Ho,<sup>4</sup> Jungfu Lin,<sup>5,\*</sup> and Renata M. Wentzcovitch<sup>3,7,8,\*</sup>

<sup>1</sup>Center for High Pressure Science and Technology Advanced Research, Beijing 100094, China

<sup>2</sup>CAS Center for Excellence in Deep Earth Science, Guangzhou 510640, China

<sup>3</sup>Department of Applied Physics and Applied Mathematics, Columbia University, New York, NY 10027, USA

<sup>4</sup>Department of Physics, Iowa State University, Ames, IA 50011, USA

<sup>5</sup>Department of Geological Sciences, Jackson School of Geosciences, The University of Texas at Austin, Austin, TX 78712, USA

<sup>6</sup>Center for Advanced Radiation Sources, University of Chicago, Chicago, IL 60439, USA

<sup>7</sup>Department of Earth and Environmental Sciences, Columbia University, New York, NY 10027, USA

<sup>8</sup>Lamont–Doherty Earth Observatory, Columbia University, Palisades, NY 10964, USA

\*These authors contributed equally

\*Correspondence: jin.liu@hpstar.ac.cn (J.L.); afu@jsg.utexas.edu (J.L.); rmw2150@columbia.edu (R.M.W.)

Received: July 22, 2022; Accepted: November 13, 2022; Published Online: November 15, 2022; <https://doi.org/10.1016/j.xinn.2022.100354>

© 2022 The Authors. This is an open access article under the CC BY-NC-ND license (<http://creativecommons.org/licenses/by-nc-nd/4.0/>).

Citation: Liu J., Sun Y., Lv C., et al., (2023). Iron-rich Fe–O compounds at Earth's core pressures. *The Innovation* 4(1), 100354.

Oxygen and iron are the most abundant elements on Earth, and their compounds are key planet-forming components. While oxygen is pervasive in the mantle, its presence in the solid inner core is still debatable. Yet, this issue is critical to understanding the co-evolution and the geomagnetic field generation. Thus far, iron monoxide (FeO) is the only known stoichiometric compound in the Fe–FeO system, and the existence of iron-rich  $\text{Fe}_n\text{O}$  compounds has long been speculated. Here, we report that iron reacts with FeO and  $\text{Fe}_2\text{O}_3$  at 220–260 GPa and 3000–3500 K in laser-heated diamond anvil cells. *Ab initio* structure searches using the adaptive genetic algorithm indicate that a series of stable stoichiometric  $\text{Fe}_n\text{O}$  compounds (with  $n > 1$ ) can be formed. Like  $\epsilon$ -Fe and B8–FeO,  $\text{Fe}_n\text{O}$  compounds have close-packed layered structures featuring oxygen-only single layers separated by iron-only layers. Two solid-solution models with compositions close to  $\text{Fe}_2\text{O}$ , the most stable Fe-rich phase identified, explain the X-ray diffraction patterns of the experimental reaction products quenched to room temperature. These results suggest that Fe-rich  $\text{Fe}_n\text{O}$  compounds with close-packed layered motifs might be stable under inner core conditions. Future studies of the elastic, rheological, and thermal transport properties of these more anisotropic  $\text{Fe}_n\text{O}$  solids should provide new insights into the seismic features of the inner core, inner core formation process and composition, and the thermal evolution of the planet.

## INTRODUCTION

The composition and the nature of the solid phases in the Earth's core remain largely uncertain.<sup>1</sup> While iron is the major component in Earth's liquid outer core (OC) and solid inner core (IC), seismology requires light elements to account for the IC and OC's "density deficit" relative to pure iron.<sup>2,3</sup> S, Si, C, H, and O are the most likely light elements in the liquid core.<sup>4</sup> Light elements may be incorporated into the solid IC as the OC continuously solidifies by forming iron-rich compounds,<sup>1,5,6</sup> such as  $\text{Fe}_7\text{C}_3$ ,  $\text{Fe}_3\text{S}$ , and  $\text{Fe}_3\text{Si}$ . High-pressure melting experiments found that eutectic Fe–FeO liquids can contain much oxygen, e.g., ~15 wt % at IC boundary conditions.<sup>7</sup> Modeling of core–mantle differentiation also indicates that oxygen is a vital light element in the liquid core.<sup>8</sup> The Fe–O system has shown rich stoichiometry under oxygen-rich conditions, e.g., the recently discovered  $\text{FeO}_2$  under lower-mantle conditions.<sup>9,10</sup> However, oxygen has been excluded from the IC because of its limited solubility in solid iron observed at low pressures and the absence of known Fe-rich Fe–O compounds.<sup>11,12</sup> The discovery of stable, solid Fe–O alloys at core pressures reported in this article changes this view, potentially impacting our understanding of the origin of the density deficit contrast between the IC and the OC and the OC composition, IC formation process, evolution, properties, etc.

Few studies have attempted to identify such O-bearing Fe-rich solids. In particular, *ab initio* studies by Sherman<sup>13</sup> and Alfè et al.<sup>14</sup> addressed substitutional and interstitial FenO structural models that were unstable against decomposition into the end members Fe and FeO. Weerasinghe et al.<sup>15</sup> performed a crystal structure search on the Fe–O system and predicted the possible existence of low-enthalpy, iron-rich FenO phases under

core pressures. Still, none have yet been synthesized at core pressures. Previous studies have shown that FeO transforms from an insulating inverse-B8 phase to a metal with the NiAs-type (B8) structure at pressures higher than 120 GPa.<sup>16,17</sup> The latter features alternating single-species (Fe-only or O-only) close-packed layers with layered motifs similar to  $\epsilon$ -Fe. Pure oxygen also becomes metallic at 96 GPa.<sup>18</sup> The change of the chemical character of FeO and O at high pressures may change their solubility in solid iron at megabar pressures.<sup>19</sup> Here, we combine high-pressure and -temperature (P-T) experiments and crystal structure predictions to search for iron-rich Fe–O compounds at pressures above 200 GPa. Because crystal structure searches identify low-temperature phases, we solve the X-ray diffraction (XRD) patterns of samples produced in P-T experiments but quenched to room temperature.

## RESULTS AND DISCUSSION

### Experimental synthesis

We performed five high-P-T experiments to synthesize  $\text{Fe}_n\text{O}$  compounds. We carried out synchrotron XRD experiments on the Fe–FeO system under high-P-T conditions using laser-heated diamond anvil cells at the Advanced Photon Source at the Argonne National Laboratory and the Shanghai Synchrotron Radiation Facility. The starting materials were mixtures of pure iron with FeO or  $\text{Fe}_2\text{O}_3$  powder in a size range of submicron to a few microns (refer to details in the material and methods). Repetitive micro-second laser pulses were employed to heat the sample for a short period of ~1 s. This laser-heating strategy significantly reduced potential carbon diffusion from the diamond anvils into the sample chamber (see Note S1). The samples were well insulated from the diamond anvils by the KCl pressure-transmitting medium and were heated up evenly on both sides to reach high temperatures readily. No reaction was observed in the first three runs at 100–200 GPa up to 2600 K (Figure S1), consistent with previous experimental studies of FeO.<sup>12,20</sup> In run 4, the Fe–FeO mixture was compressed firstly to 220 GPa at room temperature. Upon laser pulse heating to 2000–3000 K, diffraction peaks of both  $\epsilon$ -Fe and B8–FeO merely became sharper, without the appearance of any new reflections. Further laser pulse heating to 3000–3200 K showed dramatic XRD pattern changes in a few seconds (left panel in Figure S2). The integrated diffraction peak intensities of the corresponding Fe and FeO phases reduced rapidly, indicating that iron reacted with FeO above 3000 K and 220–230 GPa. A similarly rapid chemical reaction happened in run five, starting from a Fe– $\text{Fe}_2\text{O}_3$  mixture that was compressed to 200–250 GPa at room temperature and exposed to repetitive laser pulse heating. After reaching ~3000 K, the peak intensities of the Fe and  $\text{Fe}_2\text{O}_3$  phases decreased, while a set of additional diffraction peaks emerged (right panel in Figure S2). At least until 260 GPa and 3500 K, they remained unaltered before the anvils shattered upon further heating.

The diffraction peaks of the new phases did not change significantly after quenching the sample to room temperature (see Figures 1 and S2). The quenched new phase(s) remain (meta)stable at room temperature upon decompression to ~160 GPa. To improve the quality of the quenched samples'

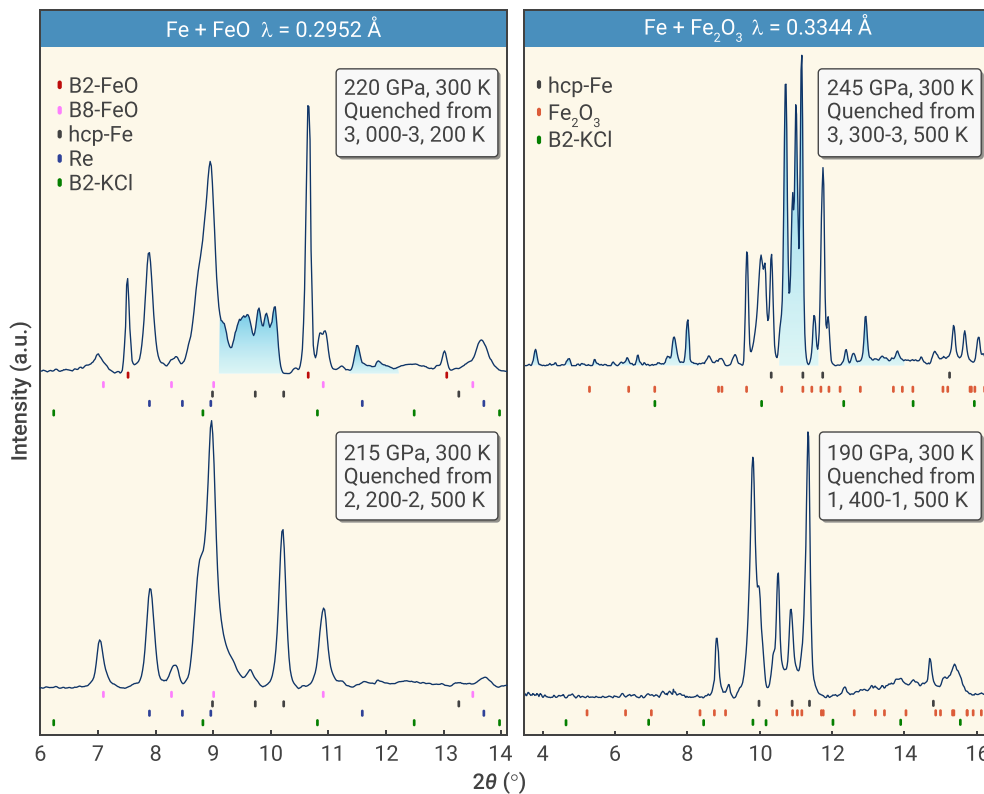


**Figure 1.** Typical X-ray diffraction patterns of quenched samples collected before and after the reaction of Fe with FeO at 220 GPa and Fe<sub>2</sub>O<sub>3</sub> at 245 GPa at high temperatures. Left panel: B8-FeO has lattice parameters  $a = 2.3480(17)$  and  $c = 4.7901(41)$  Å; hcp-Fe has  $a = 2.1792(19)$  and  $c = 3.4865(32)$  Å; hcp-Re has  $a = 2.4733(23)$  and  $c = 3.9944(47)$  Å; cubic B2-KCl has  $a = 2.7292(53)$  Å at 215–220 GPa and room temperature; B2 denotes B2-FeO. Right panel: starting materials were a mixture of iron and hematite; hcp-Fe has  $a = 2.2195(81)$  and  $c = 3.5220(115)$  Å at 190 GPa, and  $a = 2.1489(68)$  and  $c = 3.4391(95)$  Å at 245 GPa and room temperature; Fe<sub>2</sub>O<sub>3</sub> has  $a = 2.2903(57)$ ,  $b = 7.3913(116)$ , and  $c = 5.5172(81)$  Å at 190 GPa, and  $a = 2.2412(45)$ ,  $b = 7.2328(103)$ , and  $c = 5.3989(81)$  Å at 245 GPa and room temperature; cubic B2-KCl has  $a = 2.7705(64)$  Å at 190 GPa and  $a = 2.7024(71)$  Å at 245 GPa at room temperature. Vertical ticks: ε-Fe (black), B2-FeO (red), B8-FeO (magenta), post-perovskite Fe<sub>2</sub>O<sub>3</sub> (orange), B2-KCl (olive), and Re gasket (blue). Blue shaded areas highlight some of the new diffraction peaks that emerged at the expense of Fe and FeO/Fe<sub>2</sub>O<sub>3</sub> peaks when the temperature reached 3000–3200 K at 220 GPa and 3300–3500 K at 245 GPa, respectively (see Figures S3 and S4 for the indexing to the reaction products).

XRD patterns, we rotated the diamond anvil cell (DAC) by  $\pm 10^\circ$  around the incident X-ray beam direction. This procedure significantly improved the XRD peak intensities relative to the background in these polycrystalline samples (Figures S3 and S4). The short 1-s data collection time makes this procedure very challenging at high  $P$ - $T$ , and the high-temperature XRD patterns show a relatively higher background intensity (Figure S2). This was another reason for using the XRD patterns collected at room temperature and 220–245 GPa to identify the new phases. The new diffraction peaks from Fe + FeO and Fe + Fe<sub>2</sub>O<sub>3</sub> reactions show consistent  $d$  spacings (Figure S5), indicating that similar phases are produced under different experimental conditions. The new peaks could not be indexed to high-pressure phases of known oxygen-rich Fe-O compounds (e.g., Fe<sub>4</sub>O<sub>5</sub>, Fe<sub>5</sub>O<sub>6</sub>, Fe<sub>5</sub>O<sub>7</sub>, Fe<sub>2</sub>O<sub>3+δ</sub>, and FeO<sub>2</sub> in Figure S6),<sup>10,21–24</sup> or iron carbides (e.g., Fe<sub>7</sub>C<sub>3</sub> and Fe<sub>3</sub>C in Figure S7).<sup>25–27</sup>

### Crystal structure prediction

To solve the XRDs, we first conducted crystal structure searches for Fe<sub>n</sub>O ( $n > 1$ ) compounds using the adaptive genetic algorithm (AGA) at 215 GPa.<sup>28</sup> By searching in a wide range of Fe-rich compositions (see material and methods for details), several new stoichiometric Fe<sub>n</sub>O phases are found to be more stable than the combination of two end members, ε-Fe and B8-FeO. Figure 2A shows the convex hull obtained from these crystal structure searches. Four compounds with Fe<sub>3</sub>O (space group P6<sub>3</sub>/mmc), Fe<sub>2</sub>O (P $\overline{3}$ m1), Fe<sub>3</sub>O<sub>2</sub> (R $\overline{3}$ m), and Fe<sub>4</sub>O<sub>3</sub> (R $\overline{3}$ m) stoichiometries are ground states at 215 GPa. The Fe<sub>6</sub>O<sub>5</sub> (R $\overline{3}$ m) phase is very close to the convex hull, with only 0.2 meV/atom above it. All these new Fe-rich compounds have single species (Fe-only or O-only) hexagonal close-packed layers, similar to the end-member phases ε-Fe (P6<sub>3</sub>/mmc) and B8-FeO (P6<sub>3</sub>/mmc) (Figure 2B). Furthermore, most low-enthalpy compounds also have hexagonal close-packed layers, as noted by the red symbol in Figure 2A.

To study the close-packing motifs in these phases, we selected structures whose formation enthalpies are within 26 meV/atom ( $\sim 300$  K) above the convex hull. The lattice parameter  $c$  of these structures displays nearly linear dependence on the number of layers in the primitive cell (Figure 2C), suggesting a similar layered motif in all these structures. By examining these structures' stacking sequences, we found a simple compound formation rule. Only seven different three-layer stacking sequences out of 12 possible ones are present in these low-energy structures (see Figure 2D). The Fe-Fe-Fe layer sequence favors ABA stacking more than ABC, consis-

tent with the stacking in ε-Fe. Layer sequences involving oxygen, e.g., Fe-O-Fe or Fe-Fe-O, favor ABC stacking over ABA. Five arrangements involving adjacent O-O layers, e.g., Fe-O-O or O-Fe-O with ABA stacking are absent among these structures. Therefore, O-only layers are well separated from each other. This stacking rule explains why the previously proposed Fe<sub>n</sub>O models are unstable,<sup>13,14</sup> which included oxygen as substitutional and interstitial ions. The Bil<sub>3</sub>-type (R-3) model is hexagonal,<sup>14</sup> but the oxygen layers are not closely packed. All those atomic arrangements have high enthalpy. A previous computational search found an Fe<sub>3</sub>O hexagonal structure (P $\overline{6}$  m2)<sup>15</sup> more similar to the P6<sub>3</sub>/mmc ground state revealed here. However, the enthalpy of the P $\overline{6}$  m2 phase is still  $\sim 10$  meV/atom higher than the P6<sub>3</sub>/mmc phase (Figure S8). Further calculations up to IC pressures confirm the stability of P6<sub>3</sub>/mmc Fe<sub>3</sub>O against the decomposition into Fe and FeO (Figure S8). The dynamic stability of these new phases is also confirmed at both 215 and 380 GPa (Figure S9). High temperatures typical of the IC might introduce anharmonic effects that should be investigated carefully using appropriate methods for high-temperature calculations.<sup>29–31</sup>

### XRD solutions

First, we compared the predicted XRD patterns of the computationally identified Fe<sub>n</sub>O phases with the experimental ones. The four Fe<sub>n</sub>O phases in the convex hull can partially match the XRD lines of the quenched reaction products but do not provide a complete interpretation of the diffraction patterns (Figure S10). By including a few metastable Fe<sub>n</sub>O phases, the multi-phase aggregate XRD matches the experimental data better at both 220 and 245 GPa (Figure S11). Considering that all these Fe<sub>n</sub>O phases follow the same basic stacking rule, we anticipate the entropic stabilization of disordered solid solutions at high temperatures. To clarify this point, we set up reverse Monte Carlo (RMC) simulations of supercell structures with up to 60 layers ( $\sim 10$  nm) to search for the Fe/O stacking sequence that best matches the experimental XRD patterns. The interlayer distances were set using the most probable spacings found in the crystal structures identified with the AGA (see Figure 3A and refer to material and methods for more RMC simulation details).

The XRD deviation,  $D_{XRD}$ , which is the criterion used to select preferred structures during the RMC sampling, is defined as  $D_{XRD} = \sqrt{(I_{exp}(2\theta) - I_{sim}(2\theta))^2}$ , i.e., the mean-square deviation between the simulated,  $I_{sim}$ , and the experimental,  $I_{exp}$ , peak intensities. The  $2\theta$  range analyzed is restricted to  $9.2$ – $10.2^\circ$  at 220 GPa and  $10.6$ – $11.6^\circ$  at 245 GPa, corresponding to the prominent peaks of the new reaction products.

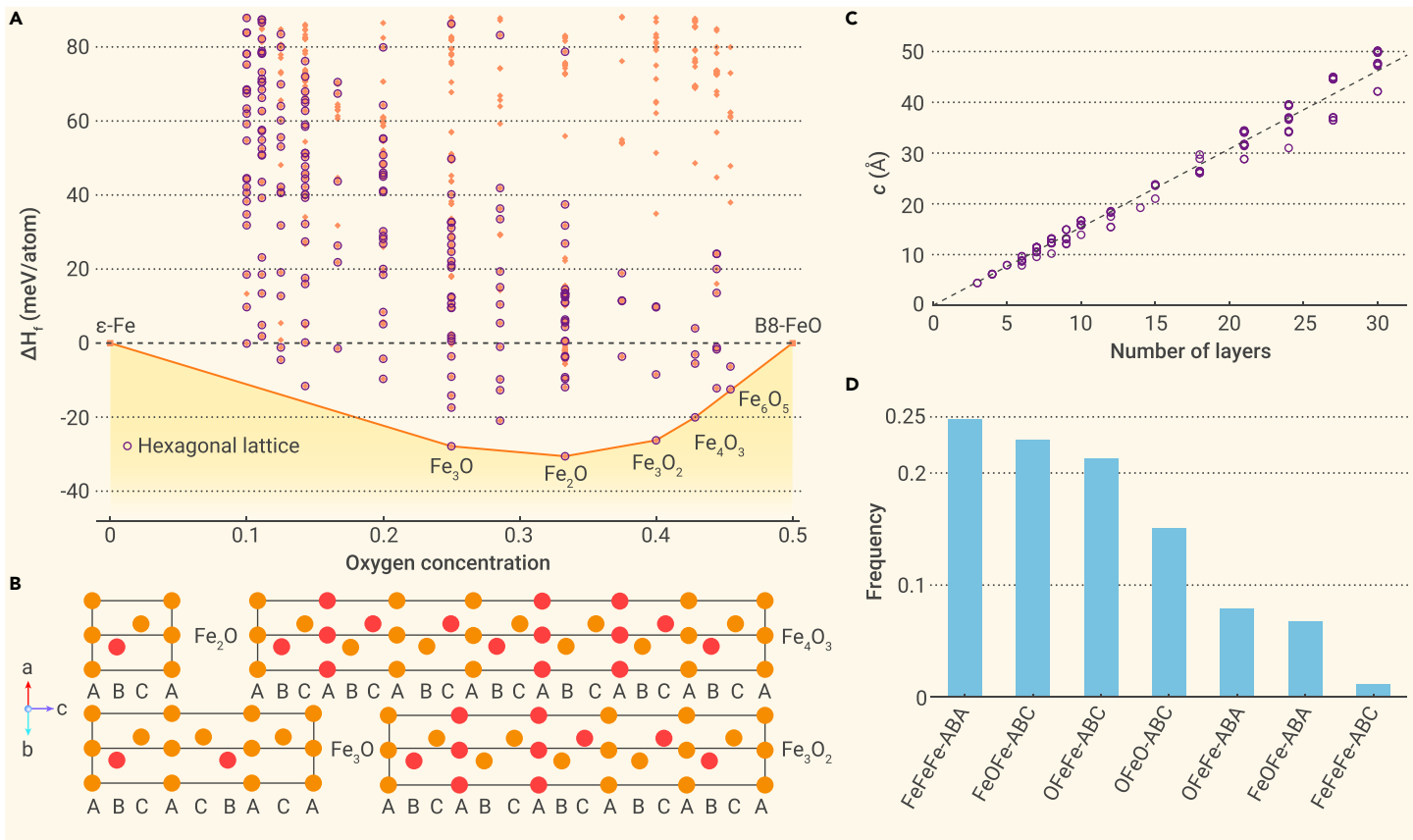


**Figure 2. Crystal structure of identified  $\text{Fe}_n\text{O}$  compounds at 215 GPa** (A) The formation enthalpy of AGA-searched compounds referenced by the dashed line shows their relative stability relative to the decomposition into  $\epsilon$ -Fe and B8-FeO. The solid line indicates the convex hull formed by the thermodynamically stable compounds. Purple circles show structures with hexagonal close-packed layers. (B) Crystal structures of four Fe-rich compounds in the ground states. Gold and red solid symbols represent iron and oxygen, respectively. (C) Lattice parameter  $c$  of low-energy close-packed crystals as a function of the number of layers. (D) Frequency of structural and chemical order in the nearest neighbor layers of the low-energy close-packed crystals.

in Figure 1. Figure 3B shows the  $D_{XRD}$  values for the different supercell sizes and iron concentrations obtained in the RMC simulations. The smallest  $D_{XRD}$  at 220 GPa points to a 42-layer structure with chemical composition  $\text{Fe}_{28}\text{O}_{14}$  shown in Figure 3C. This structure's XRD matches all additional experimental peaks of the reaction products. *Ab initio* calculations show the formation enthalpy of this phase is only 28 meV/atom above the convex hull. This supercell's calculated equation of state agrees well with the experimental one (see Note S2 and Figure S12), confirming that this structure and composition are a reasonable solution for the experimental XRD. A similar RMC was performed to solve the XRD of the reaction products of Fe and  $\text{Fe}_2\text{O}_3$  at 245 GPa (Figure S13). A 38-layer structure solution with composition  $\text{Fe}_{25}\text{O}_{13}$  can match the experimental data well, as shown in Figure S3. Analyses of these structural models indicate that they represent structures lacking long-range stacking or chemical order. However, they display medium-range structural order, i.e., domains with the preferred stacking order on the scale of  $\sim 20$  atomic layers ( $\sim 30$  Å) (see Note S3 and Figures S14–S16). Some short-range-order domains are also observed, e.g., the 5-layer sequence  $\text{FeOFeOFe}$  appears several times in Figures S15C, S15D, S16A, and S16B. The combination of and interference between the medium-range structural order domains give rise to the multi-peak patterns in the experimental XRD. The new reaction products likely consist of a disordered alloy with compositional fluctuation in the structure. The rapid temperature quench of these entropically stabilized high-temperature phases retains the disordered nature of the high-temperature phase. The high IC temperatures may favor the stabilization of these high-entropy phases. On the other hand, the long geological timescale may equilibrate an aggregate also containing the stoichiometric  $\text{Fe}_n\text{O}$  phases predicted on the convex hull. The formation of a single disordered phase versus an aggregate containing the stoichiometric  $\text{Fe}_n\text{O}$  compounds depends on the entropy versus enthalpy competi-

tion in  $\text{Fe}_n\text{O}$ , which will define the high- $P$ - $T$  Fe–FeO phase diagram at relevant conditions.

#### Electronic density of states

Figure 4 shows the electronic density of states (DOS) of  $\epsilon$ -Fe,  $\text{Fe}_3\text{O}$ ,  $\text{Fe}_2\text{O}$ , and B8-FeO at 215 GPa and  $T_{el} = 3000$  K. All  $\text{Fe}_n\text{O}$  phases discovered are metallic. In  $\epsilon$ -Fe, the Fermi level falls on a valley (Figure 4A), while in B8-FeO, it falls on a peak. Consistently, in  $\text{Fe}_n\text{O}$ , the carrier density increases systematically with increasing oxygen content. In  $\text{Fe}_2\text{O}$ , the Fermi level falls on a shallow valley, and the DOS has features resembling those of  $\epsilon$ -Fe and  $\text{FeO}$ .  $\text{Fe}_3\text{O}$  has two kinds of iron: those with (Fe1, Fe2, Fe4, Fe5) and those without (Fe3, Fe6) oxygen first neighbors (see Figure 4). Fe3-type iron's contribution to the DOS (red area in Figure 4B) resembles that of  $\epsilon$ -Fe, while Fe1-type iron's contribution (blue area in Figure 4B) resembles  $\text{Fe}_2\text{O}$ 's.

The chemical bonding nature in the  $\text{Fe}_n\text{O}$  phases is analyzed using electron localization function (ELF) and Bader charge transfer.<sup>32–34</sup> Figure 5 shows the ELF cross-sections in the (110) plane containing both Fe and O atoms for  $\epsilon$ -Fe,  $\text{Fe}_3\text{O}$ ,  $\text{Fe}_2\text{O}$ , and B8-FeO. In  $\epsilon$ -Fe, the ELF is relatively uniform. In B8-FeO, the valence electrons are more concentrated near oxygens, while Fe layers maintain a relatively uniform electron density. In  $\text{Fe}_3\text{O}$  and  $\text{Fe}_2\text{O}$ , adjacent Fe–Fe layers show similar ELFs to  $\epsilon$ -Fe, while adjacent Fe–O layers have ELFs like those in B8-FeO. Table 1 shows Bader charge transfers in these compounds. Approximately 0.97 electrons transfer from Fe to O in B8-FeO. In  $\text{Fe}_3\text{O}$  and  $\text{Fe}_2\text{O}$ , O ions gain roughly the same number of electrons, but the electron loss per Fe in  $\text{Fe}_2\text{O}$  is 0.47, i.e., half of that in  $\text{FeO}$ . In  $\text{Fe}_3\text{O}$ , Fe without O neighbors (Fe3/Fe6) shows almost no electron loss, while Fe with O neighbors (Fe1/Fe2/Fe4/Fe5) shows an electron loss of 0.45, similar to Fe in  $\text{Fe}_2\text{O}$ . Therefore, the electronic DOS, chemical bonding, and charge transfer in the  $\text{Fe}_n\text{O}$  phases can be interpreted by recalling those in the end-member phases, i.e.,  $\epsilon$ -Fe and B8-FeO. This seemingly simple and sort-of-short-range interaction between Fe and B8-FeO

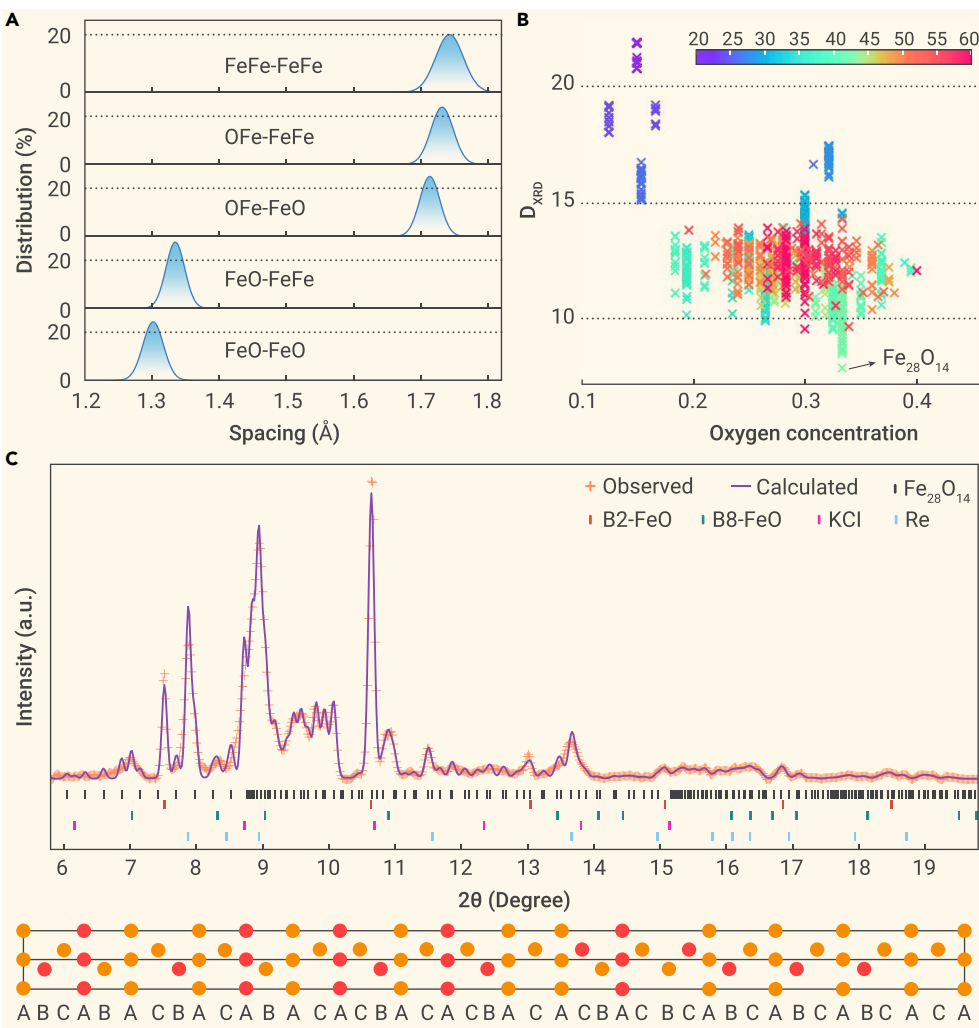


**Figure 3. Reverse Monte Carlo simulation of  $\text{Fe}_{28}\text{O}_{14}$  structure** (A) Distribution of middle-layer spacings with different neighboring layers. Legends indicate chemical elements in the first and second nearest neighbor layers, e.g., “OFe–FeO” denoting that Fe layers are the first nearest neighbor and that O layers are the second nearest neighbors. The red curve is a Gaussian distribution fitting. (B) Oxygen concentration and XRD deviation ( $D_{XRD}$ ) of supercell structures from RMC simulation. Each point represents the final structure from one RMC simulation. The color bar indicates the number of atoms in the supercell. (C) The comparison between diffraction patterns by experiments at 220 GPa and the  $\text{Fe}_{28}\text{O}_{14}$  supercell XRD produced by RMC simulations. The incident X-ray wavelength ( $\lambda$ ) is 0.2952 Å. Vertical ticks:  $\text{Fe}_{28}\text{O}_{14}$  (black),  $\text{B}2\text{-FeO}$  (orange),  $\text{B}8\text{-FeO}$  (olive),  $\text{B}2\text{-KCl}$  (magenta), and  $\text{hcp}\text{-Re}$  (blue). The lower panel shows the simulated crystal structure of  $\text{Fe}_{28}\text{O}_{14}$ .

the solid Fe-rich  $\text{Fe}_n\text{O}$  phases here suggest that the solid IC may also incorporate a significant amount of oxygen. The result is a less drastic oxygen partitioning between the OC and the IC and, consequently, a more complex origin of this density deficit contrast, with other elements also playing a significant role.<sup>8</sup> In addition, forming solid Fe-rich  $\text{Fe}_n\text{O}$  phases via IC nucleation and growth would affect the associated latent heat release from the IC to power the geodynamo through geological time.<sup>37</sup>

Oxygen has been present in every stage of Earth's formation and evolution, and chemical interactions in the deep Earth involve oxygen transfer between the core and mantle.<sup>38–40</sup> It has been suggested that the precipitation of  $\text{MgO}$ ,  $\text{FeO}$ , and  $\text{SiO}_2$  in the OC could have provided gravitational energy to drive early core convection and the Earth's ancient magnetic field before the formation of the Earth's solid

suggests that several stoichiometries are possible in the Fe–FeO system, i.e.,  $\text{Fe}_n\text{O}$  phases containing O-only and Fe-only close-packed layers stacked in different ways that depend on n. An entropically stabilized alloy with a stacking disorder is likely to form at high temperatures.

### Geophysical implications

Our high- $P$ – $T$  experiments show that Fe and  $\text{FeO}/\text{Fe}_2\text{O}_3$  react at 220–260 GPa at temperatures higher than 3000 K. At the same time, our *ab initio* crystal structure prediction identifies several stable  $\text{Fe}_n\text{O}$  phases with  $n > 1$  at similar pressure conditions. These newly identified phases differ from previously suggested  $\text{Fe}_n\text{O}$  models<sup>13,14</sup> and consist of single species (Fe-only or O-only) close-packed layers in various stacking sequences with an O-only single layer always separated by Fe-only layers. The best solutions for the experimental XRD peaks of the new phases quenched to room temperature point to structures lacking long-range chemical or stacking order. However, they still have average compositions close to  $\text{Fe}_2\text{O}$ , i.e., that of the most stable phase identified computationally in the Fe–FeO system. With this in mind, the new high-temperature reaction products are likely entropically stabilized solid solutions whose intrinsic disorder is retained upon quenching. Notably, these high-entropy phases may be favored over stoichiometric compounds (e.g.,  $\text{Fe}_2\text{O}$  and  $\text{Fe}_3\text{O}$ ) at high IC temperatures. In general, the presence of oxygen layers should make  $\text{Fe}_n\text{O}$  alloys more anisotropic from an elastic and thermal transport perspective compared with pure iron. These properties must be carefully investigated since they are essential for understanding the core's thermal evolution and seismic features, including the IC's age, energy source powering the geodynamo, and seismic heterogeneities.<sup>35,36</sup>

Oxygen has been proposed to be a likely light element alloyed with Fe in the liquid OC.<sup>8</sup> It has been postulated that an oxygen-rich liquid OC adjoining an oxygen-deprived solid IC might account for the global seismic observations of the density jump across the IC–OC boundary.<sup>11</sup> The successful syntheses of

IC.<sup>41–45</sup> The incorporation of oxygen into solid  $\text{Fe}_n\text{O}$  phase(s) extends the deep oxygen cycle to the IC and impacts this precipitation process. Future studies of multiple element partitioning, including oxygen, between solid and liquid Fe will help clarify the relative abundances of the light elements, the origin of the density deficit in both regions, and many other processes involving the Earth's core evolution.

### MATERIALS AND METHODS

#### Sample preparation and characterization

The starting materials of pure iron (C.A.S. #7439-89-6) mixed with  $\text{FeO}$  (C.A.S. #1345-25-1) or  $\text{Fe}_2\text{O}_3$  (C.A.S. #1309-37-1) powders with grain sizes ranging from submicron to a few microns were prepared in an Fe/O ratio ~3:1. Each of the two mixtures was mechanically ground for 90 min in a glove box filled with Ar. Pairs of single- or double-beveled diamond anvils with culet sizes of 50–300 or 60–180–300  $\mu\text{m}$  were used for the laser-heated DAC experiments. The sample disk of each Fe–O mixture was compressed to ~3- $\mu\text{m}$  thick and 14–16  $\mu\text{m}$  across and was selected and loaded into a sample chamber measuring 20–25  $\mu\text{m}$  across consisting of a pre-indented Re gasket. Each sample platelet was sandwiched between two dried KCl platelets used as the pressure-transmitting medium and thermal insulation layers. The whole DAC sample assembly was sealed in a vacuum using a high-pressure gas loading system after being evacuated for 30 min before each sample chamber was compressed to high pressures. Before reaching a target pressure, XRD patterns were collected at ~30 GPa to confirm the presence of both iron and iron oxide.

#### Synchrotron XRD experiments

High- $P$ – $T$  XRD measurements were conducted at beamlines 13-IDD of the Advanced Photon Source, Argonne National Laboratory. A highly monochromatized X-ray source with an energy of 42 keV (0.2952 Å) was used as the incident X-ray beam and focused

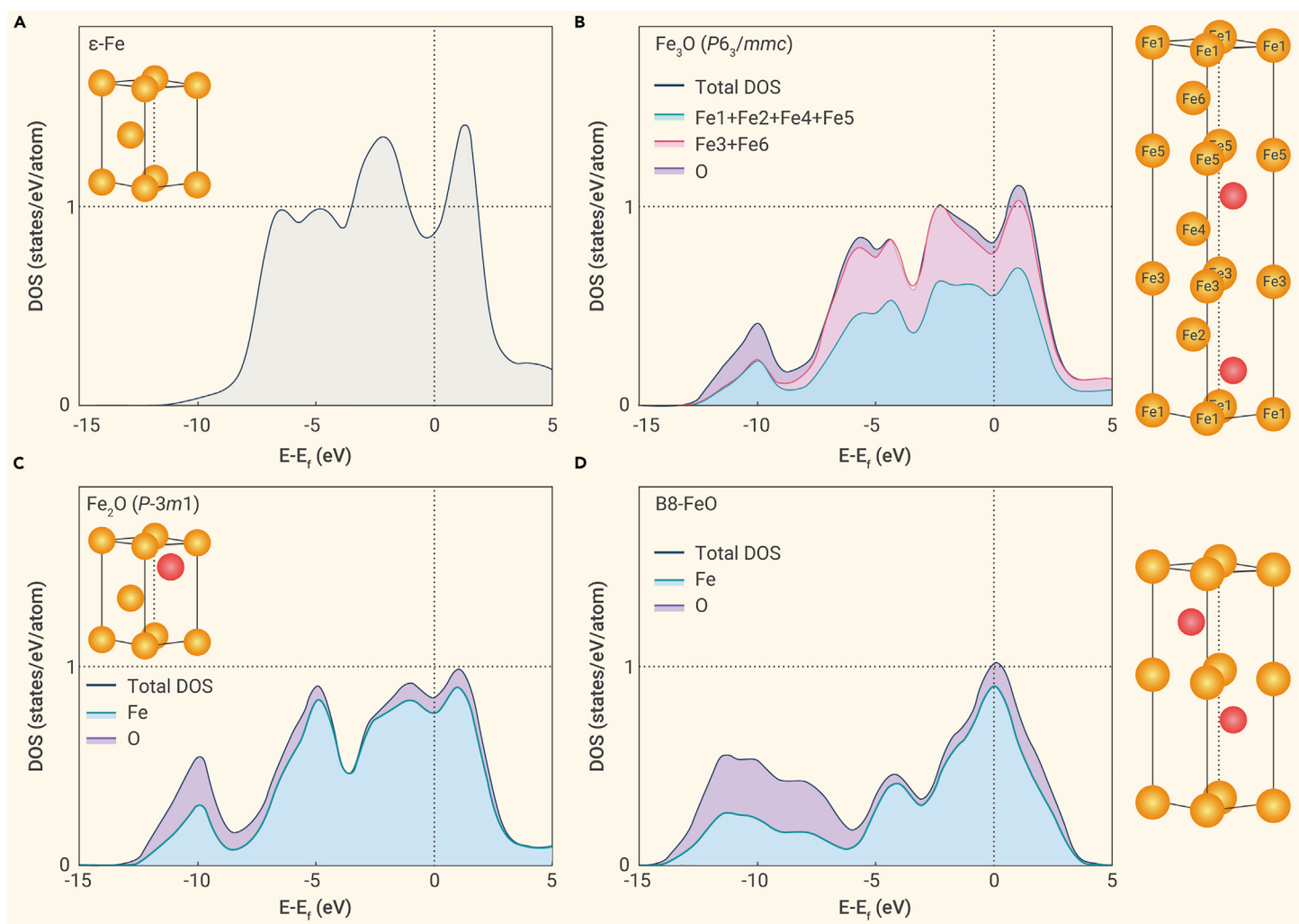


**Figure 4.** Projected DOS of Fe 3d electrons in Fe and  $\text{Fe}_n\text{O}$  compounds at 220 GPa and  $T_{\text{el}} = 3,000$  K (A)  $\epsilon$ -Fe. The dashed line indicates the Fermi level. (B)  $\text{Fe}_3\text{O}$  (space group  $P6_3/mmc$ ). The blue area shows the partial DOS of Fe ions with oxygen neighbor layers (i.e., Fe1, Fe2, Fe4, and Fe5 shown in the crystal structure), while the magenta area shows the partial DOS of Fe ions without oxygen neighbors (Fe3, Fe6). The purple area shows the partial DOS of O. (C)  $\text{Fe}_2\text{O}$  ( $P\bar{3}m1$ ). (D) B8- $\text{FeO}$ . Gold and red spheres represent iron and oxygen ions, respectively. The DOS is normalized by dividing the total number of atoms in the cell.

down to a 2- to 5- $\mu\text{m}$  spot size (full width at half maximum) at the sample position. Each DAC was compressed to high pressure at room temperature in preparation for the laser heating experiments. The pressure was determined from the lattice parameters of hcp-Fe and B2-KCl, generally with an uncertainty of 2–5 GPa.<sup>46</sup> At targeted pressures, two infrared laser beams were focused on 20- to 30- $\mu\text{m}$  spots (full width at half maximum) on both sides of the sample. They were co-axially aligned with the incident X-ray beam using the X-ray-induced luminescence on the sample and/or ruby. We estimated the temperature of the heated samples by fitting measured thermal radiation spectra with the gray-body assumption function. The temperature uncertainty was within 100–200 K based on multiple temperature measurements on both sides.

#### AGA search

We searched for crystal structures of Fe-rich  $\text{Fe}_n\text{O}$  using the AGA,<sup>28,47,48</sup> which combines *ab initio* calculations and auxiliary interatomic potentials described by the embedded-atom method in an adaptive manner to ensure high efficiency and accuracy. The structure searches were only constrained by the chemical composition, without any assumption on the Bravais lattice type, symmetry, atom basis, or unit cell dimensions. A wide range of different Fe-rich compositions (i.e., 2:1, 3:1, 3:2, 4:1, 4:3, 5:1, 5:2, 5:3, 5:4, 6:1, 6:5, 7:1, 8:1, 9:1) were selected with up to 25 atoms in the unit cell to perform the search. Each AGA run contains a genetic algorithm (GA) loop accelerated by interatomic potential and a density functional theory (DFT) calculation loop to refine the potential. The candidate pool in the GA search contained 64 structures. In each GA generation, 16 new structures were generated from the parent structure pool via the mating procedure. The structures in the pool were updated by keeping 64 of the lowest-energy structures. The structure search with a given auxiliary interatomic potential sustained 1000 consecutive GA generations. After one GA loop, 16

structures were randomly selected for the static DFT calculation to refine the potential. This process was repeated 80 times, followed by DFT structure optimization on unique crystal structures.

#### Ab initio calculations

We conducted *ab initio* calculations using the projector augmented-wave (PAW) method within DFT, as implemented in the VASP code.<sup>49–51</sup> The exchange and correlation energies were treated with the generalized gradient approximation parameterized by the Perdew–Burke–Ernzerhof formula.<sup>52</sup> PAW potentials with valence electronic configurations  $3d^74s1$  and  $2s^22p^4$  were used for the Fe and O atoms, respectively. The hard-core PAW potential with  $3s^23p^63d^74s1$  for Fe was also tested. Both Fe PAWs show consistent results (see Note S4 and Figure S17). The Mermin functional was employed.<sup>53,54</sup> A plane-wave basis set was used with a kinetic energy cutoff of 650 eV. During the AGA search, the Monkhorst–Pack sampling scheme was adopted for Brillouin zone sampling with a  $k$ -point grid of  $2\pi \times 0.033 \text{ \AA}^{-1}$ ,<sup>55</sup> and the ionic relaxations stopped when the forces on every atom became smaller than 0.01 eV/ $\text{\AA}$ . The energy convergence criterion is  $10^{-4}$  eV. Phonon calculations were performed using density functional perturbation theory implemented in the VASP code and the Phonopy software,<sup>56,57</sup> with a  $k$ -point grid of  $2\pi \times 0.033 \text{ \AA}^{-1}$  and supercells of  $3 \times 3 \times 2$  for  $\text{Fe}_2\text{O}$  (54 atoms),  $2 \times 2 \times 2$  for  $\text{Fe}_3\text{O}$  (64 atoms),  $2 \times 2 \times 2$  for  $\text{Fe}_3\text{O}_2$  rhombohedral lattice (40 atoms), and  $2 \times 2 \times 2$  for  $\text{Fe}_4\text{O}_3$  rhombohedral lattice (56 atoms).

#### RMC simulations

The RMC simulations were performed by randomly changing the chemistry (Fe/O ratio) and layer stackings in the supercells of the hexagonal lattice. There is no restriction

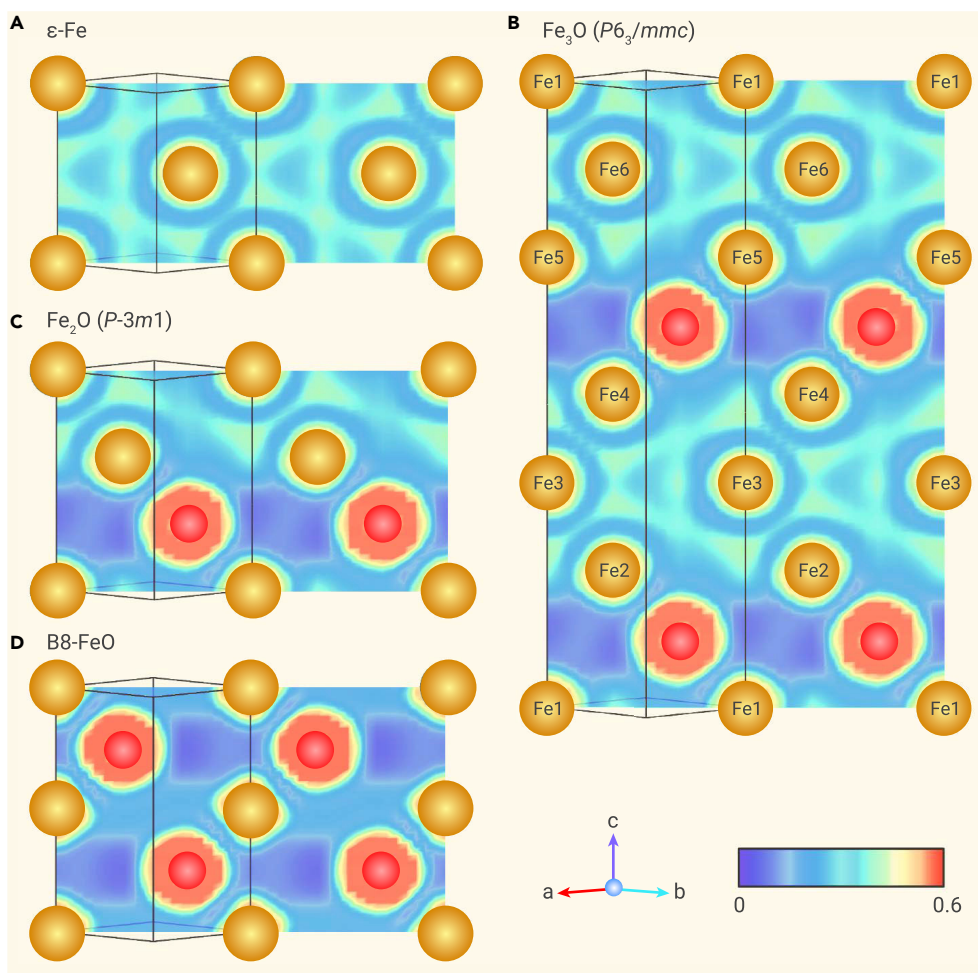


**Figure 5.** Electron localization function (A)  $\epsilon$ -Fe, (B)  $\text{Fe}_3\text{O}$  (space group  $P6_3/mmc$ ), (C)  $\text{Fe}_2\text{O}$  ( $P\bar{3}m1$ ), and (D) B8-FeO. Gold and red spheres represent iron and oxygen, respectively.

of the overall Fe/O concentration in the supercell. The only criterion to select preferred structures during the random sampling is based on the XRD deviation  $D_{XRD} = \sqrt{(I_{exp}(2\theta) - I_{sim}(2\theta))^2}$ , which is the mean-square deviation of the intensities between simulated,  $I_{sim}$ , and experimental,  $I_{exp}$ , XRDs. The smaller the  $D_{XRD}$ , the better the agreement with the experimental data. The acceptance rate during the RMC simulation follows the typical Metropolis acceptance rule as  $p = e^{-\beta\Delta D}$ , where  $\Delta D$  is the change of XRD deviation between two MC steps.  $\beta$  is a scaling factor that makes the overall acceptance rate around 20%. The structure is updated if the stacking changes during the RMC simulation. The interlayer distances were set using the most probable spacings shown in Figure 3A. According to Figure 2D, only seven out of 12 stacking sequences appeared in the low-energy structures found with the AGA search. Stackings other than the seven preferred ones in the RMC simulations were discouraged by assigning large  $\Delta D$ s. The RMC simulations used supercells containing 20 to 60 layers. Each simulation was repeated independently 30 times.

#### Data availability

All original data supporting the findings and structure files of this study have been deposited at <https://doi.org/10.5281/zenodo.7155153>.

**Table 1.** Bader charge analysis of the  $\text{Fe}_n\text{O}$  phases

| Phase                                  | Fe  | O     |
|--|---|-------|
| $\epsilon$ -Fe                         | 0   | –     |
| $\text{Fe}_3\text{O}$ ( $P6_3/mmc$ )   | Fe1/Fe2/Fe4/Fe5: +0.45,<br>Fe3/Fe6: +0.01 | –0.91 |
| $\text{Fe}_2\text{O}$ ( $P\bar{3}m1$ ) | +0.47                                     | –0.94 |
| B8-FeO                                 | +0.97                                     | –0.97 |

The indices of Fe in  $\text{Fe}_3\text{O}$  correspond to those in Figures 4B and 5.

#### REFERENCES

- Hirose, K., Labrosse, S., and Hernlund, J. (2013). Composition and state of the core. *Annu. Rev. Earth Planet Sci.* **41**, 657–691.
- Birch, F. (1952). Elasticity and constitution of the Earth's interior. *J. Geophys. Res.* **57**, 227–286.
- Poirier, J.-P. (1994). Light elements in the Earth's outer core: a critical review. *Phys. Earth Planet. In.* **85**, 319–337.
- Hirose, K., Wood, B., and Vočadlo, L. (2021). Light elements in the Earth's core. *Nat. Rev. Earth Environ.* **2**, 645–658.
- Morard, G., Andraut, D., Antonangeli, D., and Bouchet, J. (2014). Properties of iron alloys under the Earth's core conditions. *Compt. Rendus Geosci.* **346**, 130–139.
- Lin, J.-F., Heinz, D.L., Campbell, A.J., et al. (2002). Iron-silicon alloy in Earth's core? *Science* **295**, 313–315.
- Oka, K., Hirose, K., Tagawa, S., et al. (2019). Melting in the Fe-FeO system to 204 GPa: implications for oxygen in Earth's core. *Am. Mineral.* **104**, 1603–1607.
- Badro, J., Brodholt, J.P., Piet, H., et al. (2015). Core formation and core composition from coupled geochemical and geophysical constraints. *Proc. Natl. Acad. Sci. USA* **112**, 12310–12314.
- Hu, Q., Kim, D.Y., Yang, W., et al. (2016).  $\text{FeO}_2$  and  $\text{FeOOH}$  under deep lower-mantle conditions and Earth's oxygen-hydrogen cycles. *Nature* **534**, 241–244.
- Liu, J., Hu, Q., Bi, W., et al. (2019). Altered chemistry of oxygen and iron under deep Earth conditions. *Nat. Commun.* **10**, 153.
- Alfè, D., Gillan, M.J., and Price, G.D. (2000). Constraints on the composition of the Earth's core from ab initio calculations. *Nature* **405**, 172–175.
- Ozawa, H., Hirose, K., Tateno, S., et al. (2010). Phase transition boundary between B1 and B8 structures of FeO up to 210 GPa. *Phys. Earth Planet. In.* **179**, 157–163.
- Sherman, D.M. (1995). Stability of possible Fe-FeS and Fe-FeO alloy phases at high pressure and the composition of the Earth's core. *Earth Planet. Sci. Lett.* **132**, 87–98.
- Alfè, D., Price, G., and Gillan, M.J. (1999). Oxygen in the Earth's core: a first-principles study. *Phys. Earth Planet. In.* **110**, 191–210.
- Weerasinghe, G.L., Pickard, C.J., and Needs, R.J. (2015). Computational searches for iron oxides at high pressures. *J. Phys. Condens. Matter* **27**, 455501.
- Fei, Y., and Mao, H.K. (1994). *In situ* determination of the NiAs phase of FeO at high pressure and temperature. *Science* **266**, 1678–1680.
- Ozawa, H., Hirose, K., Ohta, K., et al. (2011). Spin crossover, structural change, and metallization in NiAs-type FeO at high pressure. *Phys. Rev. B* **84**, 134417.

18. Weck, G., Desgreniers, S., Loubeyre, P., and Mezouar, M. (2009). Single-crystal structural characterization of the metallic phase of oxygen. *Phys. Rev. Lett.* **102**, 255503.
19. Ringwood, A.E., and Hibberson, W. (1990). The system Fe-FeO revisited. *Phys. Chem. Miner.* **17**, 313–319.
20. Ozawa, H., Takahashi, F., Hirose, K., et al. (2011). Phase transition of FeO and stratification in Earth's outer core. *Science* **334**, 792–794.
21. Lavina, B., Dera, P., Kim, E., et al. (2011). Discovery of the recoverable high-pressure iron oxide  $\text{Fe}_4\text{O}_5$ . *Proc. Natl. Acad. Sci. USA* **108**, 17281–17285.
22. Lavina, B., and Meng, Y. (2015). Unraveling the complexity of iron oxides at high pressure and temperature: synthesis of  $\text{Fe}_5\text{O}_6$ . *Sci. Adv.* **1**, e1400260.
23. Bykova, E., Dubrovinsky, L., Dubrovinskaya, N., et al. (2016). Structural complexity of simple  $\text{Fe}_2\text{O}_3$  at high pressures and temperatures. *Nat. Commun.* **7**, 10661.
24. Liu, J., Wang, C., Lv, C., et al. (2021). Evidence for oxygenation of Fe-Mg oxides at mid-mantle conditions and the rise of deep oxygen. *Natl. Sci. Rev.* **8**, nwaa096.
25. Chen, B., Li, Z., Zhang, D., et al. (2014). Hidden carbon in Earth's inner core revealed by shear softening in dense  $\text{Fe}_3\text{C}$ . *Proc. Natl. Acad. Sci. USA* **111**, 17755–17758.
26. Prescher, C., Dubrovinsky, L., Liu, X., et al. (2015). High Poisson's ratio of Earth's inner core explained by carbon alloying. *Nat. Geosci.* **8**, 220–223.
27. Liu, J., Lin, J., Prakapenka, V.B., et al. (2016). Phase relations of  $\text{Fe}_3\text{C}$  and  $\text{Fe}_2\text{C}_3$  up to 185 GPa and 5200 K: Implication for the stability of iron carbide in the Earth's core. *Geophys. Res. Lett.* **43**, 12415–12422.
28. Wu, S.Q., Ji, M., Wang, C.Z., et al. (2014). An adaptive genetic algorithm for crystal structure prediction. *J. Phys. Condens. Matter* **26**, 035402.
29. Zhang, Z., Zhang, D.B., Sun, T., and Wentzcovitch, R. (2019). phq: a Fortran code to compute phonon quasiparticle properties and dispersions. *Comput. Phys. Commun.* **243**, 110–120.
30. Sun, Y., Mendelev, M.I., Zhang, F., et al. (2022). Ab Initio Melting Temperatures of Bcc and Hcp Iron under the Earth's Inner Core Condition. Preprint at arXiv. <https://doi.org/10.48550/arXiv.2205.02290>.
31. Zhang, D.-B., Sun, T., and Wentzcovitch, R.M. (2014). Phonon quasiparticles and anharmonic free energy in complex systems. *Phys. Rev. Lett.* **112**, 058501.
32. Becke, A.D., and Edgecombe, K.E. (1990). A simple measure of electron localization in atomic and molecular systems. *J. Chem. Phys.* **92**, 5397–5403.
33. Silvi, B., and Savin, A. (1994). Classification of chemical bonds based on topological analysis of electron localization functions. *Nature* **371**, 683–686.
34. Henkelman, G., Arnaldsson, A., and Jónsson, H. (2006). A fast and robust algorithm for Bader decomposition of charge density. *Comput. Mater. Sci.* **36**, 354–360.
35. Hsieh, W.-P., Goncharov, A.F., Labrosse, S., et al. (2020). Low thermal conductivity of iron-silicon alloys at Earth's core conditions with implications for the geodynamo. *Nat. Commun.* **11**, 3332.
36. Zhang, Y., Hou, M., Liu, G., et al. (2020). Reconciliation of experiments and theory on transport properties of iron and the geodynamo. *Phys. Rev. Lett.* **125**, 078501.
37. O'Rourke, J.G., Korenaga, J., and Stevenson, D.J. (2017). Thermal evolution of Earth with magnesium precipitation in the core. *Earth Planet. Sci. Lett.* **463**, 263–272.
38. Knittle, E., and Jeanloz, R. (1991). Earth's core-mantle boundary: results of experiments at high pressures and temperatures. *Science* **251**, 1438–1443.
39. Takafuji, N., Hirose, K., Mitome, M., and Bando, Y. (2005). Solubilities of O and Si in liquid iron in equilibrium with  $(\text{Mg}, \text{Fe})\text{SiO}_3$  perovskite and the light elements in the core. *Geophys. Res. Lett.* **32**, L06313.
40. Tsuno, K., Frost, D.J., and Rubie, D.C. (2013). Simultaneous partitioning of silicon and oxygen into the Earth's core during early Earth differentiation. *Geophys. Res. Lett.* **40**, 66–71.
41. O'Rourke, J.G., and Stevenson, D.J. (2016). Powering Earth's dynamo with magnesium precipitation from the core. *Nature* **529**, 387–389.
42. Badro, J., Siebert, J., and Nimmo, F. (2016). An early geodynamo driven by exsolution of mantle components from Earth's core. *Nature* **536**, 326–328.
43. Hirose, K., Morard, G., Sinmyo, R., et al. (2017). Crystallization of silicon dioxide and compositional evolution of the Earth's core. *Nature* **543**, 99–102.
44. Davies, C.J., Pozzo, M., Gubbins, D., and Alfè, D. (2020). Transfer of oxygen to Earth's core from a long-lived magma ocean. *Earth Planet. Sci. Lett.* **538**, 116208.
45. Zhang, Z., Csányi, G., Alfè, D., et al. (2022). Free energies of Fe-O-Si ternary liquids at high temperatures and pressures: implications for the evolution of the Earth's core composition. *Geophys. Res. Lett.* **49**, e2021GL096749.
46. Dewaele, A., Belonoshko, A.B., Garbarino, G., et al. (2012). High-pressure–high-temperature equation of state of KCl and KBr. *Phys. Rev. B* **85**, 214105.
47. Deaven, D.M., and Ho, K.M. (1995). Molecular geometry optimization with a genetic algorithm. *Phys. Rev. Lett.* **75**, 288–291.
48. Zhao, X., Nguyen, M.C., Zhang, W., et al. (2014). Exploring the structural complexity of intermetallic compounds by an adaptive genetic algorithm. *Phys. Rev. Lett.* **112**, 045502.
49. Blöchl, P.E. (1994). Projector augmented-wave method. *Phys. Rev. B Condens. Matter* **50**, 17953–17979.
50. Kresse, G., and Furthmüller, J. (1996). Efficiency of ab-initio total energy calculations for metals and semiconductors using a plane-wave basis set. *Comput. Mater. Sci.* **6**, 15–50.
51. Kresse, G., and Furthmüller, J. (1996). Efficient iterative schemes for ab initio total-energy calculations using a plane-wave basis set. *Phys. Rev. B Condens. Matter* **54**, 11169–11186.
52. Perdew, J.P., Burke, K., and Ernzerhof, M. (1996). Generalized gradient approximation made simple. *Phys. Rev. Lett.* **77**, 3865–3868.
53. Mermin, N.D. (1965). Thermal properties of the inhomogeneous electron gas. *Phys. Rev.* **137**, A1441–A1443.
54. Wentzcovitch, R.M., Martins, J.L., and Allen, P.B. (1992). Energy versus free-energy conservation in first-principles molecular dynamics. *Phys. Rev. B Condens. Matter* **45**, 11372–11374.
55. Monkhorst, H.J., and Pack, J.D. (1976). Special points for Brillouin-zone integrations. *Phys. Rev. B* **13**, 5188–5192.
56. Baroni, S., de Gironcoli, S., Dal Corso, A., and Giannozzi, P. (2001). Phonons and related crystal properties from density-functional perturbation theory. *Rev. Mod. Phys.* **73**, 515–562.
57. Togo, A., and Tanaka, I. (2015). First principles phonon calculations in materials science. *Scr. Mater.* **108**, 1–5.

## ACKNOWLEDGMENTS

This work is supported by NSFC grants nos. 42072052 and U1930401 and by National Science Foundation awards EAR-1918126 (R.M.W. and Y.S.), EAR-1918134 (K.H. and C.W.), and EAR-1901808 and EAR-1916941 (J. Lin). R.M.W. also acknowledges partial support from the Department of Energy, Theoretical Chemistry Program, through grant DE-SC0019759. Computational resources were provided by the Extreme Science and Engineering Discovery Environment (XSEDE) funded by the National Science Foundation through award ACI-1548562. This research also used resources of the Advanced Photon Source, a US Department of Energy Office of Science User Facility operated by Argonne National Laboratory under contract no. DE-AC02-06CH11357. The GeoSoilEnviroCARS at the Advanced Photon Source is supported by the National Science Foundation - Earth Sciences award EAR-1634415 and the Department of Energy-GeoSciences award DE-FG02-94ER14466. Some experiments are supported by the Synergic Extreme Condition User Facility (SECUF) and beamline BL15U1 at the Shanghai Synchrotron Radiation Facility (SSRF).

## AUTHOR CONTRIBUTIONS

J. Lin, J. Liu, R.M.W., and Y.S. conceived the project. Y.S., F.Z., C.W., and K.H. performed *ab initio* calculations and crystal structure search. J. Liu, J. Lin, C.L., S.F., and V.B.P. carried out synchrotron experiments and data analyses. J. Liu, Y.S., and R.M.W. wrote the manuscript. All authors discussed the results and contributed to paper writing.

## DECLARATION OF INTERESTS

The authors declare no competing interests.

## SUPPLEMENTAL INFORMATION

Supplemental information can be found online at <https://doi.org/10.1016/j.xinn.2022.100354>.

## LEAD CONTACT WEBSITE

<https://www.jsg.utexas.edu/lin>  
<http://mineralscloud.org/>

**Supplemental Information**

**Iron-rich Fe–O compounds at Earth's core pressures**

**Jin Liu, Yang Sun, Chaojia Lv, Feng Zhang, Suyu Fu, Vitali B. Prakapenka, Caizhuang Wang, Kaiming Ho, Jungfu Lin, and Renata M. Wentzcovitch**

## Supplementary Information

### Iron-rich Fe-O compounds at Earth's core pressures

Jin Liu,<sup>1,2,9,\*</sup> Yang Sun,<sup>3,9</sup> Chaojia Lv,<sup>1</sup> Feng Zhang,<sup>4</sup>, Suyu Fu,<sup>5</sup> Vitali B. Prakapenka,<sup>6</sup> Caizhuang Wang,<sup>4</sup> Kaiming Ho,<sup>4</sup> Jungfu Lin,<sup>5,\*</sup> and Renata M. Wentzcovitch<sup>3,7,8,\*</sup>

<sup>1</sup>Center for High Pressure Science and Technology Advanced Research, Beijing 100094, China

<sup>2</sup>CAS Center for Excellence in Deep Earth Science, Guangzhou 510640, China

<sup>3</sup>Department of Applied Physics and Applied Mathematics, Columbia University, New York, NY 10027, USA

<sup>4</sup>Department of Physics, Iowa State University, Ames, Iowa 50011, USA

<sup>5</sup>Department of Geological Sciences, Jackson School of Geosciences, The University of Texas at Austin, Austin, TX 78712, USA

<sup>6</sup>Center for Advanced Radiation Sources, University of Chicago, Chicago, IL 60439, USA

<sup>7</sup>Department of Earth and Environmental Sciences, Columbia University, New York, NY 10027, USA

<sup>8</sup>Lamont–Doherty Earth Observatory, Columbia University, Palisades, NY 10964, USA

<sup>\*</sup>These authors contributed equally

\*Correspondence: jin.liu@hpstar.ac.cn (J.L.); afu@jsg.utexas.edu (J.L.); rmw2150@columbia.edu (R. W.)

## SUPPLEMENTARY MATERIALS

Supplementary Notes 1-4

Supplementary References 1-14

Supplementary Figures S1-S17

### **Supplementary Note 1 | Experimental XRD patterns and the examination of Fe-C solution.**

We employed repetitive laser pulses to reduce the likelihood of breaking diamond anvils significantly. Short heating durations of a few  $\mu\text{s}$  in each pulse reduce carbon diffusion and contamination from the sample chamber by the diamond anvils. A few XRD patterns obtained from different experimental conditions and post-analysis are shown in Figs. S1–S7. Fig. S1 shows the XRD without reaction at 183 GPa and 2,000 K. Fig. S2 shows high-pressure and high-temperature XRDs at  $\sim$ 200–260 GPa, 2,200–3,500 K. Figs. S3 and S4 show room-temperature XRDs with the  $\text{Fe}_{25}\text{O}_{13}$  and  $\text{Fe}_{28}\text{O}_{14}$  solutions, respectively. Fig. S5 shows the room-temperature XRD of quenched samples in *d*-spacing units. Fig. S6 shows the comparison between room-temperature XRD and known oxygen-rich  $\text{FeO}$  compounds.

To rule out the possibility of a reaction between Fe and C from the DAC, we compare in Fig. S7 XRD patterns of known Fe-C compounds with the experimental XRD data at room temperature and 220 GPa and 245 GPa.  $\text{Fe}_3\text{C}$  (*Pnma*) and  $\text{Fe}_7\text{C}_3$  (*Pbca*) are the two main Fe-C compounds stable under high *P-T* conditions relevant to our experiments.<sup>1-3</sup> At 220 GPa, neither  $\text{Fe}_3\text{C}$  nor  $\text{Fe}_7\text{C}_3$  can explain the prominent unrecognized diffraction peaks in the 9.6 to 10.2 degrees range. At 245 GPa,  $\text{Fe}_3\text{C}$  or  $\text{Fe}_7\text{C}_3$  cannot explain the unrecognized diffraction peaks in the 11.0 to 11.3 degrees range either. These factors exclude the two Fe-C phases as the main reason for the additional XRD peaks in the current data.

### **Supplementary Note 2 | Equation of states of the close-packed $\text{Fe}_n\text{O}$ phases.**

To further validate the supercell model of  $\text{Fe}_{28}\text{O}_{14}$ , we compared its static equation of state (EoS) with the experimental data collected upon decompression at room temperature (Fig. S12). The comparison demonstrates the current model well describes the compressive behavior of the reaction product. The slightly smaller calculated volumes of  $\text{Fe}_{28}\text{O}_{14}$  are expected owing to the absence of vibrational effects in the calculation.<sup>4</sup> The  $\text{Fe}_{28}\text{O}_{14}$  model is too large and anisotropic to perform phonon calculations with the frozen phonon method or density functional perturbation theory. Therefore, to evaluate the vibrational contribution, we use the  $\text{Fe}_2\text{O}$  ground state structure (*P $\bar{3}m$ 1* phase in the main text) and compute the static and the 300K EoSs using the quasiharmonic approximation (QHA).<sup>5</sup> The vibrational effect on the EoS of  $\text{Fe}_2\text{O}$  at 300 K is shown in Fig. S12. A similar effect is anticipated in the EoS of  $\text{Fe}_{28}\text{O}_{14}$ , which improves agreement between calculated and measured volumes at 300 K. The difference between the static volumes of the  $\text{Fe}_{28}\text{O}_{14}$  structure

model and Fe<sub>2</sub>O can be attributed to the disordered nature of Fe<sub>28</sub>O<sub>14</sub>. The remaining difference is typical of *ab initio* calculations.

### **Supplementary Note 3 | Chemical and structural orders in the Fe<sub>n</sub>O close-packed hexagonal lattices.**

We analyzed the chemical and structural orders of the supercells obtained from Reverse Monte Carlo (RMC) simulations (Fig. 3 in the main text and Fig. S13) to explore the meaning of these solutions. We smeared the iron density profile along the *c* direction using a Gaussian with FWHM of 9.0 Å, corresponding to ~6-layer spacings. Figure S14 shows that the Fe<sub>28</sub>O<sub>14</sub> and Fe<sub>25</sub>O<sub>13</sub> structures have significant compositional variations in the nanometer scale ranging from Fe<sub>5</sub>O<sub>2</sub> to Fe<sub>3</sub>O<sub>2</sub>. Although the average Fe/O ratio of the initial Fe-FeO sample mixture was 3:1, the laser-heated spot centered around a FeO-rich area and the main reaction product appears to have a composition of Fe<sub>2</sub>O or nearly so. This is not surprising since Fe<sub>2</sub>O is the most stable (with the lowest formation enthalpy) composition in the convex hull. Still, without knowing the phase diagram in detail, it is impossible to predict if the reaction would have followed to completion to produce a phase with an average composition of Fe<sub>3</sub>O had the sample been heated longer. The fast reaction process likely causes compositional fluctuations during the short laser heating period. Rapid quenching of an entropically stabilized high-temperature phase also contributes to the observed disorder.

A characteristic feature of the XRD patterns at 220 and 245 GPa is their multi-peaks structure in a small  $2\theta$  range. To explore the origin of these peaks, we plot the corresponding lattice planes in the supercell. As shown in Fig. S15a and b, the three main XRD peaks at 220 GPa correspond to the Miller indices (0,1,18), (0,1,-17), and (0,1,16). The main peaks at 245 GPa correspond to indices (0,1,14), (0,1,-13) and (0,1,-11). The corresponding lattice planes are shown in Fig. S15c and d. Visual examination of these structures reveals multi-layer domains with distinct stacking types. They are more easily distinguished by tilting the paper and examining these figures horizontally with the line of sight parallel to the lines specifying the crystalline planes. In both cases, two major domains can be identified in Fig. S16a and b. In Fe<sub>28</sub>O<sub>14</sub>, domain A is Fe<sub>16</sub>O<sub>8</sub>, while domain B is Fe<sub>12</sub>O<sub>6</sub>. They contribute differently to the peak intensities. As shown in Fig. S16c, domain A mainly contributes to (0,1,18) and (0,1,-17) peaks, while domain B largely contributes to (0,1,16) and (0,1,14) peaks. Neither of the single domains can fully describe the

XRD. Interference among them is also important as it leads to the suppression of the (0,1,15) peak. Similar behavior is observed in the Fe<sub>25</sub>O<sub>13</sub> supercell in Fig. S16d.

These analyses conclude that these supercell solutions represent structures lacking long-range stacking or chemical order. However, they display medium-range structural order (MRO), i.e., domains with preferred stacking order but lacking chemical order at the scale of ~20 atomic layers or ~30 Å. Similar structures have been observed in layered alloys produced from high-temperature solid solutions.<sup>6</sup> The combination and interferences of the MRO domains give rise to complex multi-peak patterns in the current experimental XRD.

#### **Supplementary Note 4 | Consistency of PAW potentials.**

We used projector augmented wave (PAW) potentials from the VASP software with the valence electron of  $3d^74s^1$  for Fe (noted as PAW8) and  $2s^22p^4$  for O. This PAW8 potential is more efficient for the structure optimization in the crystal structure prediction algorithm with thousands of structures. PAW8 was previously used to discover FeO<sub>2</sub> and showed predictive accuracy.<sup>7</sup>

Here, we study the effect of PAW potential by comparing the enthalpy of the Fe<sub>n</sub>O compounds using the hard-core Fe potential with valence electron of  $3s^23p^63d^74s^1$  (noted as PAW16). Fig. S17a shows that using PAW16, the enthalpy values of the predicted lowest-enthalpy structures are systematically lower than those predicted using PAW8. However, it is the enthalpy of formation that determines relative stabilities. The formation enthalpies calculated by the two PAW potentials differ by less than ~3 meV/atom, as shown in Fig. S17b. Both PAW potentials produce similar convex hulls. Therefore, PAW8 is sufficiently accurate to describe the Fe<sub>n</sub>O phases at pressures of interest.

## Supplementary References

1. Prescher, C., Dubrovinsky, L., Bykova, E. et al. (2015). High Poisson's ratio of Earth's inner core explained by carbon alloying. *Nat. Geosci.* **8**, 220-223.
2. Chen, B., Li, Z., Zhang, D. et al. (2014). Hidden carbon in Earth's inner core revealed by shear softening in dense Fe<sub>7</sub>C<sub>3</sub>. *Proc. Natl. Acad. Sci. U.S.A.* **111** 17755-17758.
3. Liu, J., Lin, J. F., Prakapenka, V. B., Prescher, C., and Yoshino, T. (2016). Phase relations of Fe<sub>3</sub>C and Fe<sub>7</sub>C<sub>3</sub> up to 185 GPa and 5200 K: Implication for the stability of iron carbide in the Earth's core. *Geophys. Res. Lett.* **43**, 12415-12422.
4. Wentzcovitch, R. M., Yu, Y. G., and Wu, Z. (2010). Thermodynamic properties and phase relations in mantle minerals investigated by first principles quasiharmonic theory. *Rev. Mineral. Geochem.* **71**, 59-98.
5. Qin, T., Zhang, Q., Wentzcovitch, R. M., and Umemoto, K. (2019). qha: A Python package for quasiharmonic free energy calculation for multi-configuration systems. *Comput. Phys. Commun.* **237**, 199-207.
6. Palasyuk, O., Onyszczak, M., Kim, T.-H. et al. (2021). Structural and magnetic properties of hard magnetic system Ce(Co<sub>1-x</sub>Fe<sub>x</sub>)<sub>4.4</sub>Cu<sub>0.6</sub> (0 ≤ x ≤ 0.19). *J. Alloys Compd.* **883**, 160866.
7. Hu, Q., Kim, D. Y., Yang, W. et al. (2016). FeO<sub>2</sub> and FeOOH under deep lower-mantle conditions and Earth's oxygen-hydrogen cycles. *Nature* **534**, 241-244.
8. Lavina, B., Dera, P., Kim, E. et al. (2011). Discovery of the recoverable high-pressure iron oxide Fe<sub>4</sub>O<sub>5</sub>. *Proc. Natl. Acad. Sci. U.S.A.* **108**, 17281-17285.
9. Lavina, B., and Meng, Y. (2015). Unraveling the complexity of iron oxides at high pressure and temperature: Synthesis of Fe<sub>5</sub>O<sub>6</sub>. *Sci. Adv.* **1**, e1400260.
10. Bykova, E., Dubrovinsky, L., Dubrovinskaia, N. et al. (2016). Structural complexity of simple Fe<sub>2</sub>O<sub>3</sub> at high pressures and temperatures. *Nat. Commun.* **7**, 10661.
11. Liu, J., Wang, C., Lv, C. et al. (2021). Evidence for oxygenation of Fe-Mg oxides at mid-mantle conditions and the rise of deep oxygen. *Natl. Sci. Rev.* **8**, nwaa096.
12. Liu, J., Hu, Q., Bi, W. et al. (2019). Altered chemistry of oxygen and iron under deep Earth conditions. *Nat. Commun.* **10**, 153.
13. Weerasinghe, G. L., Pickard, C. J., and Needs, R. J. (2015). Computational searches for iron oxides at high pressures. *J. Phys.: Condens. Matter* **27**, 455501.
14. Alfè, D., Gillan, M. J., and Price, G. D. (2007). Temperature and composition of the Earth's core. *Contemp. Phys.* **48**, 63-80.

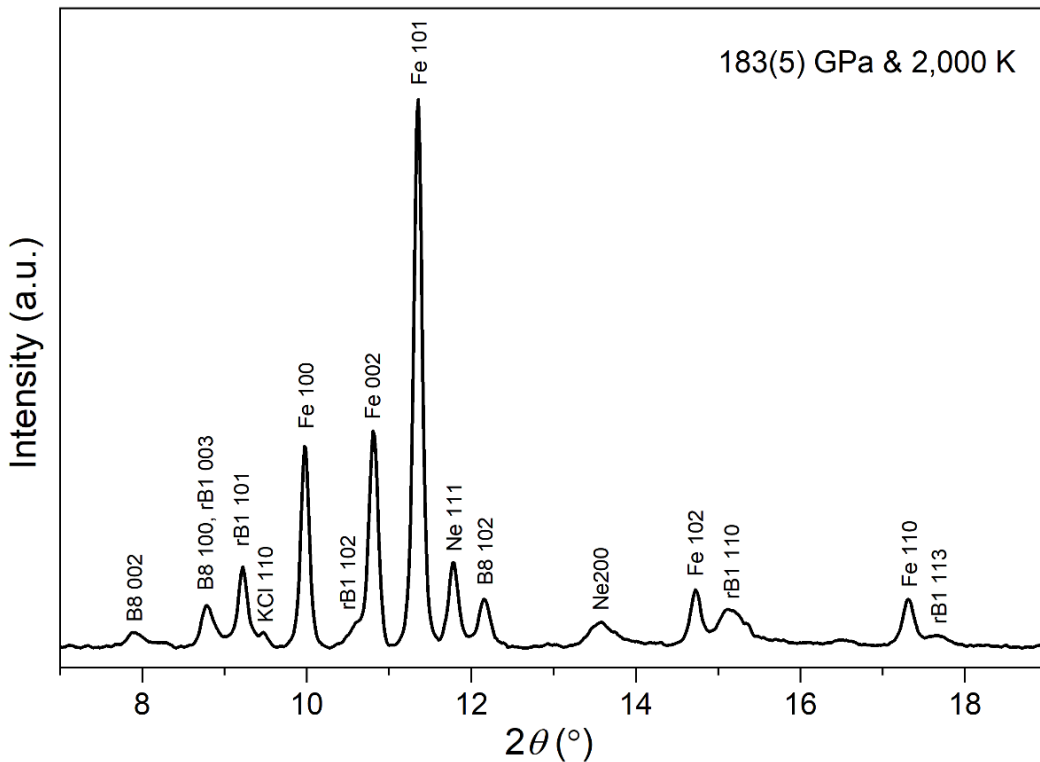


**Figure S1 | Representative x-ray diffraction pattern collected at 183 GPa and 2000 K.** A mixture of Fe and FeO was used as starting materials. B8 and rB1 labels denote the NiAs-type (B8) and rhombohedral (rB1) phases of FeO, respectively. The x-ray wavelength ( $\lambda$ ) used is 0.3344 Å. Known structures explain all peaks.

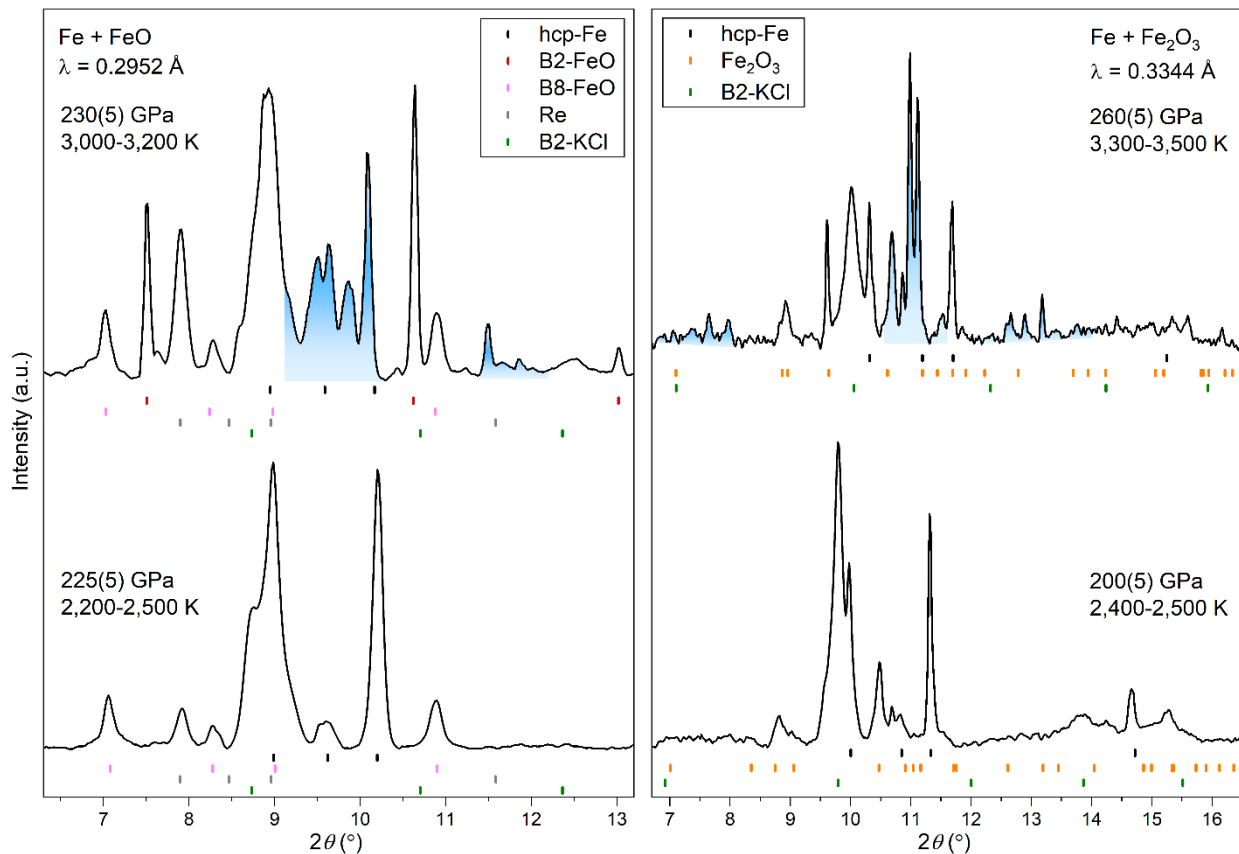


**Figure S2 | Representative x-ray diffraction patterns collected at simultaneously high-pressure and high-temperature conditions before and after the reaction of Fe with FeO (left) and  $\text{Fe}_2\text{O}_3$  (right).** Left panel: The mixture of polycrystalline Fe and FeO was used as starting material. B2 and B8 labels denote the CsCl-type (B2) and NiAs-type (B8) phases of FeO, respectively. The x-ray wavelength ( $\lambda$ ) used is  $0.2952 \text{ \AA}$ . Right panel: The mixture of polycrystalline Fe and  $\text{Fe}_2\text{O}_3$  was used as starting material, with KCl used as the pressure-transmitting medium and pressure calibrant. The x-ray wavelength ( $\lambda$ ) used is  $0.3344 \text{ \AA}$ . The blue areas highlight some of the new diffraction peaks that emerged at the expense of Fe and FeO peaks when the temperature reached 3,000–3,200 K at pressures greater than 220 GPa. Vertical ticks:  $\epsilon$ -Fe (black), B2-FeO (red), B8-FeO (magenta), post-perovskite  $\text{Fe}_2\text{O}_3$  (orange), B2-KCl (olivine), and Re gasket (grey).

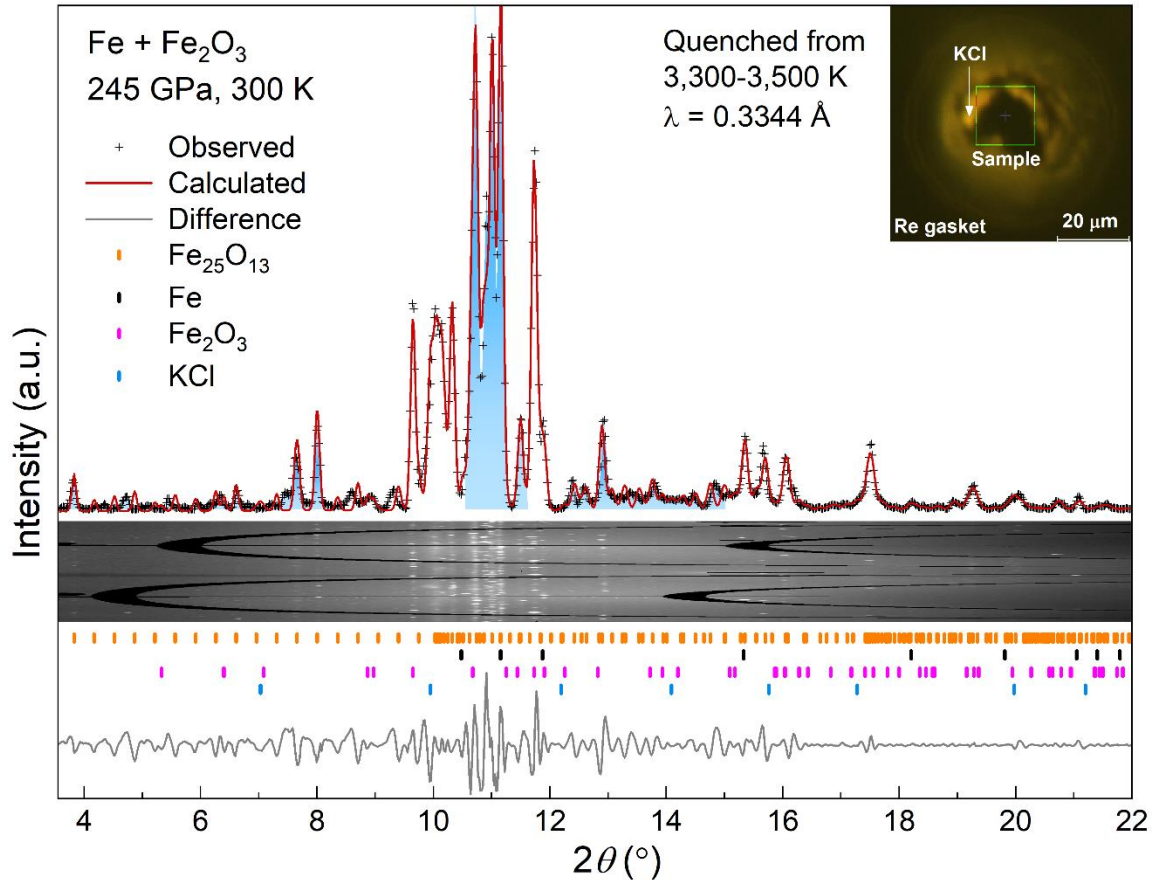


**Figure S3 | Representative XRD pattern of iron and hematite  $\text{Fe}_2\text{O}_3$  reaction products at core pressures at 245 GPa.** The pattern at 245 GPa was collected at room temperature after the laser-heated sample was quenched from 3,300–3,500 K at 250–260 GPa. The red curve denotes the Le Bail refinements, whereas the gray line represents the refinement residue. Vertical ticks: hexagonal  $\text{Fe}_{25}\text{O}_{13}$  (orange),  $\varepsilon$ -Fe (black), post-perovskite  $\text{Fe}_2\text{O}_3$  (magenta), and B2-KCl (blue). The mixture of polycrystalline Fe and  $\alpha$ - $\text{Fe}_2\text{O}_3$  (hematite) was used as starting material. KCl served as pressure calibrant and thermal insulation, as shown in the inset. Re is the gasket material. The x-ray wavelength ( $\lambda$ ) was 0.3344 Å. The blue areas highlight some of the new diffraction peaks. The  $\text{Fe}_{25}\text{O}_{13}$  supercell has  $a = 2.2082(34)$  Å and  $c = 55.082(49)$  Å; cubic B2-KCl has  $a = 2.7024(71)$  Å;  $\text{Fe}_2\text{O}_3$  (space group:  $\text{Cmcm}$ ) has  $a = 2.2379(45)$  Å,  $b = 7.1934(103)$  Å and  $c = 5.4094(81)$  Å; hcp-Fe has  $a = 2.1489(68)$  Å and  $c = 3.4391(95)$  Å.

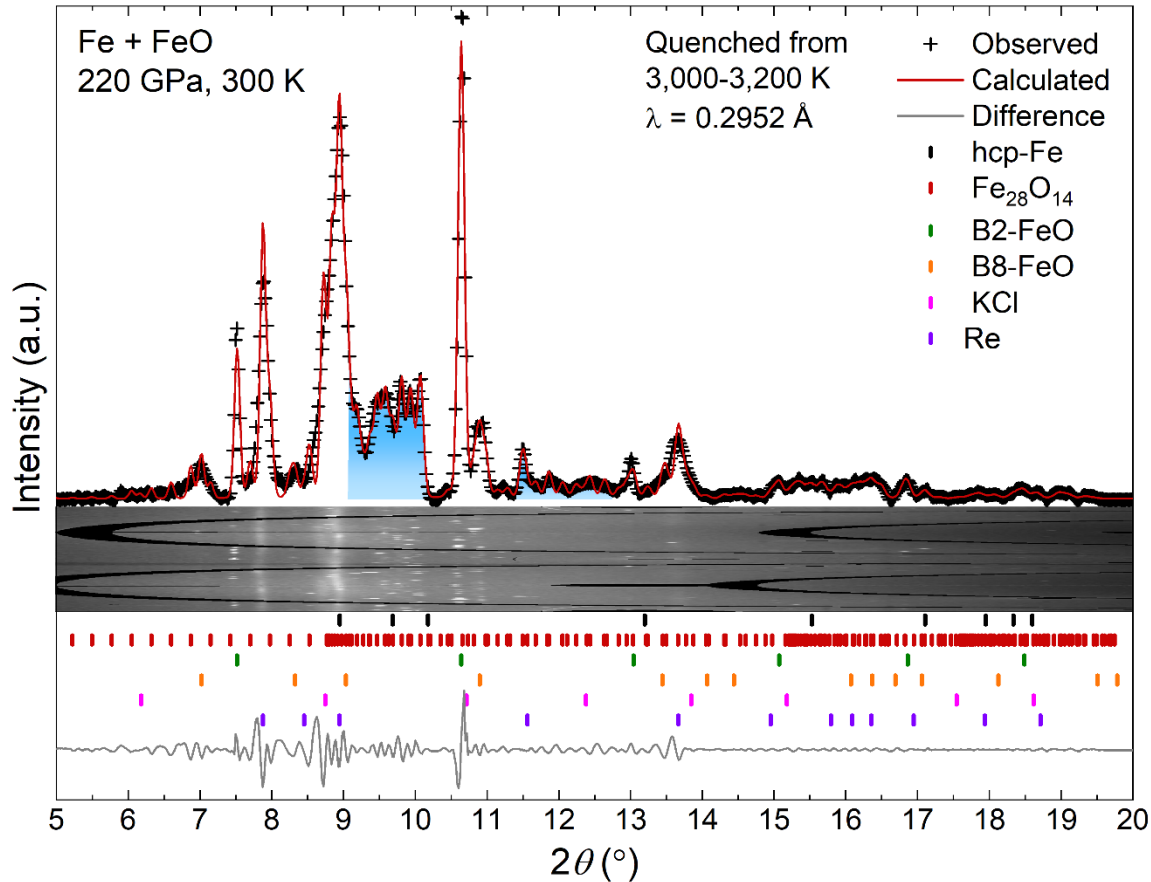


**Figure S4 | Representative XRD pattern of iron and wüstite (FeO) reaction products at 220 GPa.** The pattern at 220 GPa was collected at room temperature after the laser-heated sample was quenched from 3,000–3,200 K at 230–235 GPa. The new phase(s) emerged at the expense of Fe and FeO when the temperature surpassed 3,000 K. B8-FeO has lattice parameters  $a = 2.3480(17)$  Å and  $c = 4.7901(41)$  Å; hcp-Fe has  $a = 2.1792(19)$  Å and  $c = 3.4865(32)$  Å; hcp-Re has  $a = 2.4733(23)$  Å and  $c = 3.9944(47)$  Å; cubic B2-KCl has  $a = 2.7292(53)$  Å; The  $\text{Fe}_{28}\text{O}_{14}$  supercell has  $a = 2.2287(45)$  Å and  $c = 61.546(78)$  Å. The blue areas highlight some of the new diffraction peaks.

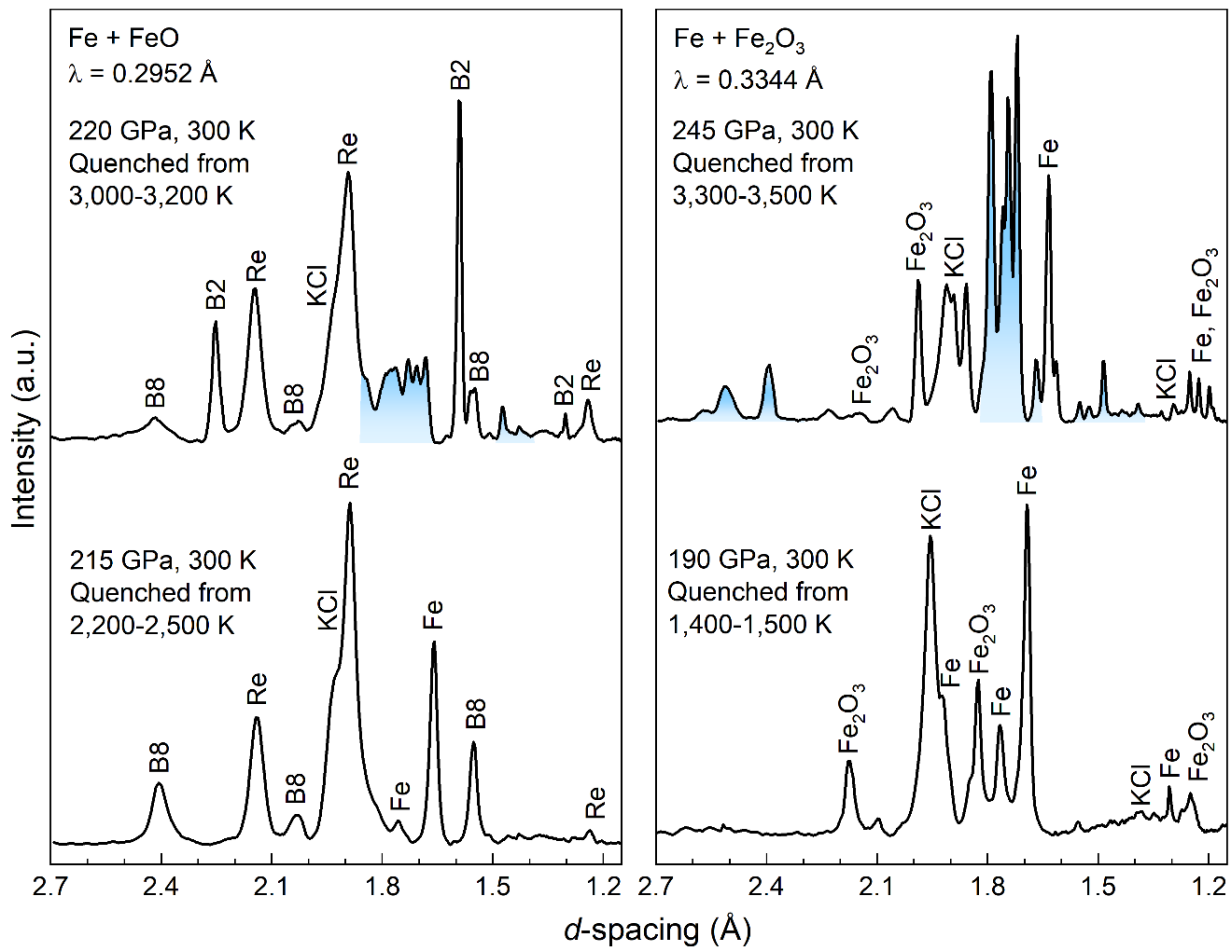


**Figure S5 | Room-temperature x-ray diffraction patterns as a function of the *d*-spacing from the reaction of Fe with FeO (left) and Fe<sub>2</sub>O<sub>3</sub> (right).** The blue areas highlight some of the new diffraction peaks that emerged at the expense of Fe and FeO/Fe<sub>2</sub>O<sub>3</sub> peaks when the temperature reached 3,000–3,200 at 220 GPa and 3,300–3,500 K at 245 GPa, respectively. Left panel: B8-FeO has lattice parameters  $a = 2.3480(17) \text{ \AA}$  and  $c = 4.7901(41) \text{ \AA}$ ; hcp-Fe has  $a = 2.1792(19) \text{ \AA}$  and  $c = 3.4865(32) \text{ \AA}$ ; hcp-Re has  $a = 2.4733(23) \text{ \AA}$  and  $c = 3.9944(47) \text{ \AA}$ ; cubic B2-KCl has  $a = 2.7292(53) \text{ \AA}$ ; B2 denotes B2-FeO. Right panel: Starting materials were iron and hematite (Fe<sub>2</sub>O<sub>3</sub>). The pattern is obtained by transforming  $2\theta$  in Fig. 1 to *d*-spacing.

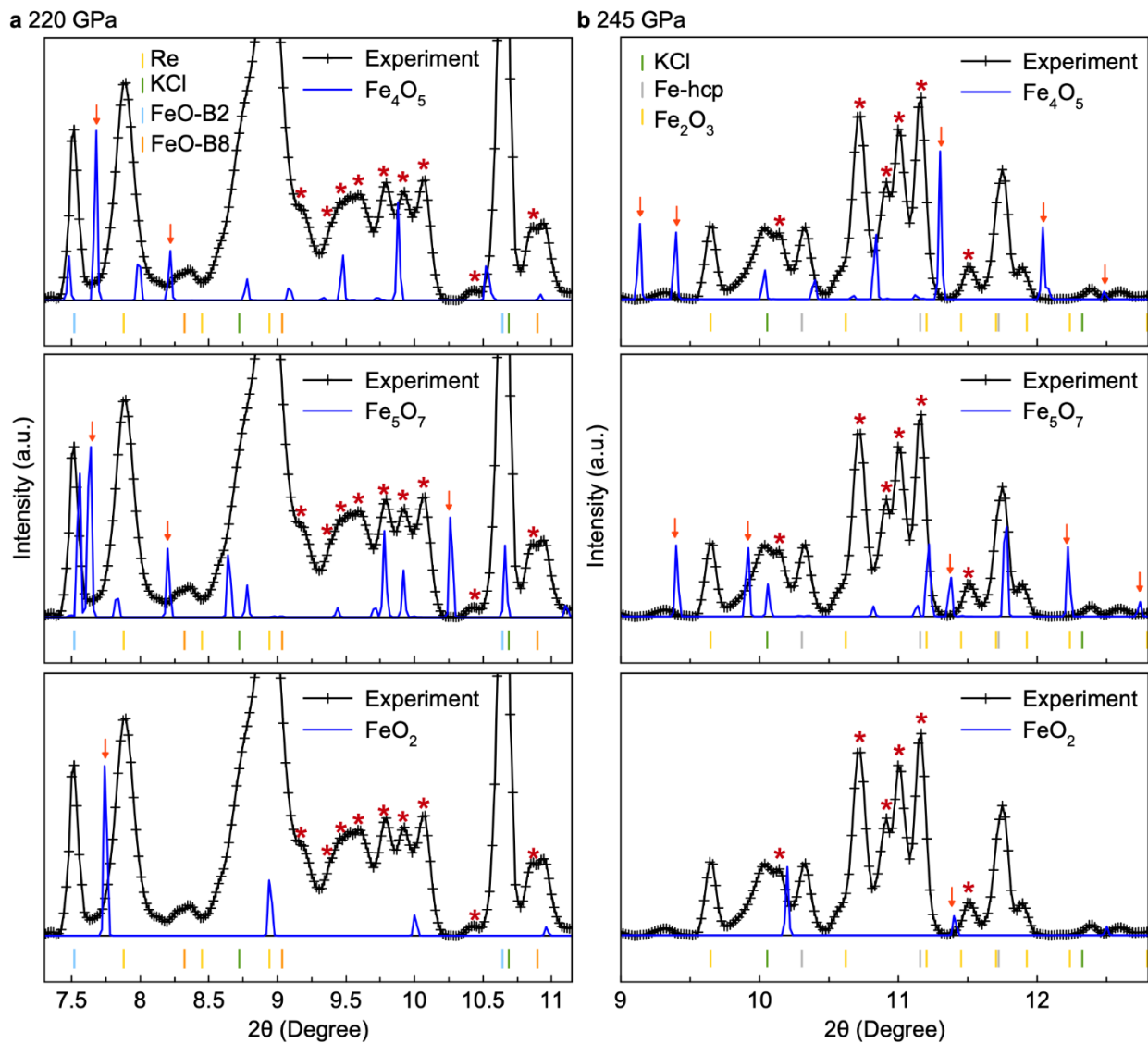


**Figure S6 | Comparison between experimental x-ray diffraction patterns and those of oxygen-rich Fe-O compounds.** The XRD patterns were collected from (a) Fe+FeO reaction at 220 GPa and (b) Fe+Fe<sub>2</sub>O<sub>3</sub> reaction at 245 GPa at room temperature. Blue lines indicate the XRD of oxygen-rich Fe-O compounds.<sup>8-12</sup> Arrows indicate extra peaks of oxygen-rich Fe-O compounds. The x-ray wavelength ( $\lambda$ ) was 0.2952 Å for the reaction product of Fe and FeO at 220 GPa, and that was 0.3344 Å for the reaction product of Fe and Fe<sub>2</sub>O<sub>3</sub> at 245 GPa. The asterisk symbol (\*) represents the diffraction peak of the new phase. No oxygen-rich Fe-O phase could match new experimental diffraction peaks.

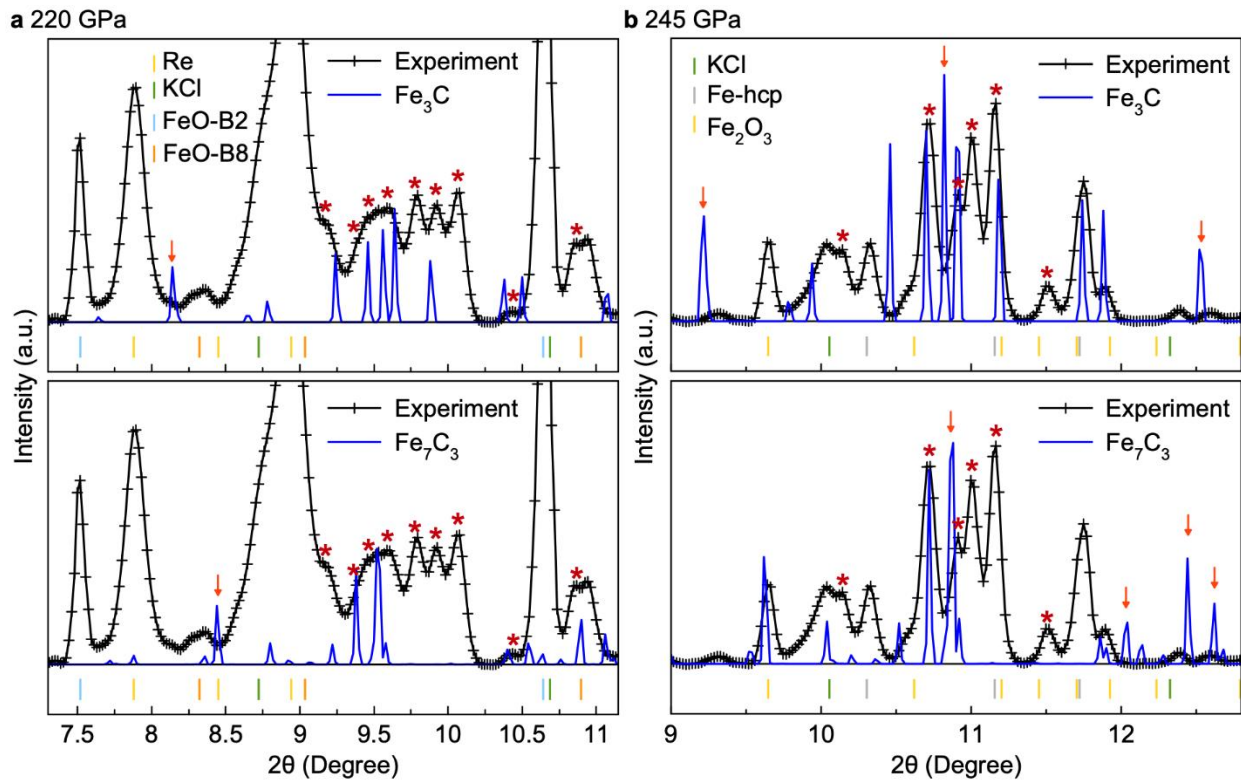


**Figure S7 | Comparison between experimental X-ray diffraction patterns and those of  $\text{Fe}_3\text{C}/\text{Fe}_7\text{C}_3$ .** The patterns were collected from (a)  $\text{Fe}+\text{FeO}$  reaction at 220 GPa and (b)  $\text{Fe}+\text{Fe}_2\text{O}_3$  reaction at 245 GPa. Arrows indicate extra peaks of the  $\text{Fe}_3\text{C}/\text{Fe}_7\text{C}_3$  phases. The x-ray wavelength ( $\lambda$ ) was 0.2952 Å for the reaction product of  $\text{Fe}$  and  $\text{FeO}$  at 220 GPa, and that was 0.3344 Å for the reaction product of  $\text{Fe}$  and  $\text{Fe}_2\text{O}_3$  at 245 GPa. The asterisk symbol (\*) represents the diffraction peak of the new phases.

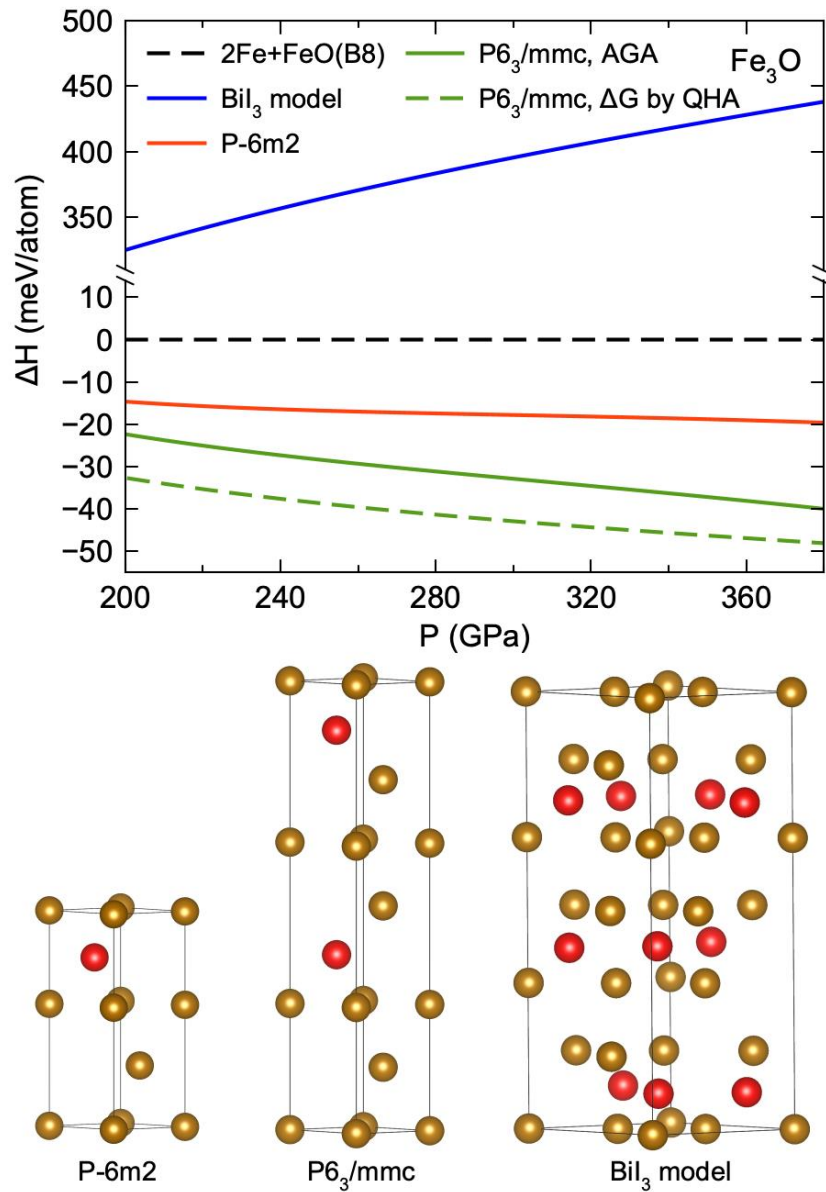


**Figure S8 | Relative enthalpy of  $\text{Fe}_3\text{O}$  models.** The  $P-6m2$  and  $\text{BiI}_3$ -type ( $R-3$ ) phases are from Weerasinghe *et al.*<sup>13</sup> and Alfè *et al.*<sup>14</sup>, respectively. The relative enthalpy is referenced to the decomposition products  $\varepsilon\text{-Fe}$  and  $\text{B8-FeO}$ . The lower panel shows the atomic structures. The Fe-O-Fe layer stacking in the  $P-6m2$  phase is ABA while it is ABC in the  $P6_3/mmc$  phase. The dashed line shows the relative Gibbs free energy ( $\Delta G$ ) of  $P6_3/mmc$  phase computed with quasiharmonic approximation (QHA) at 3000 K.

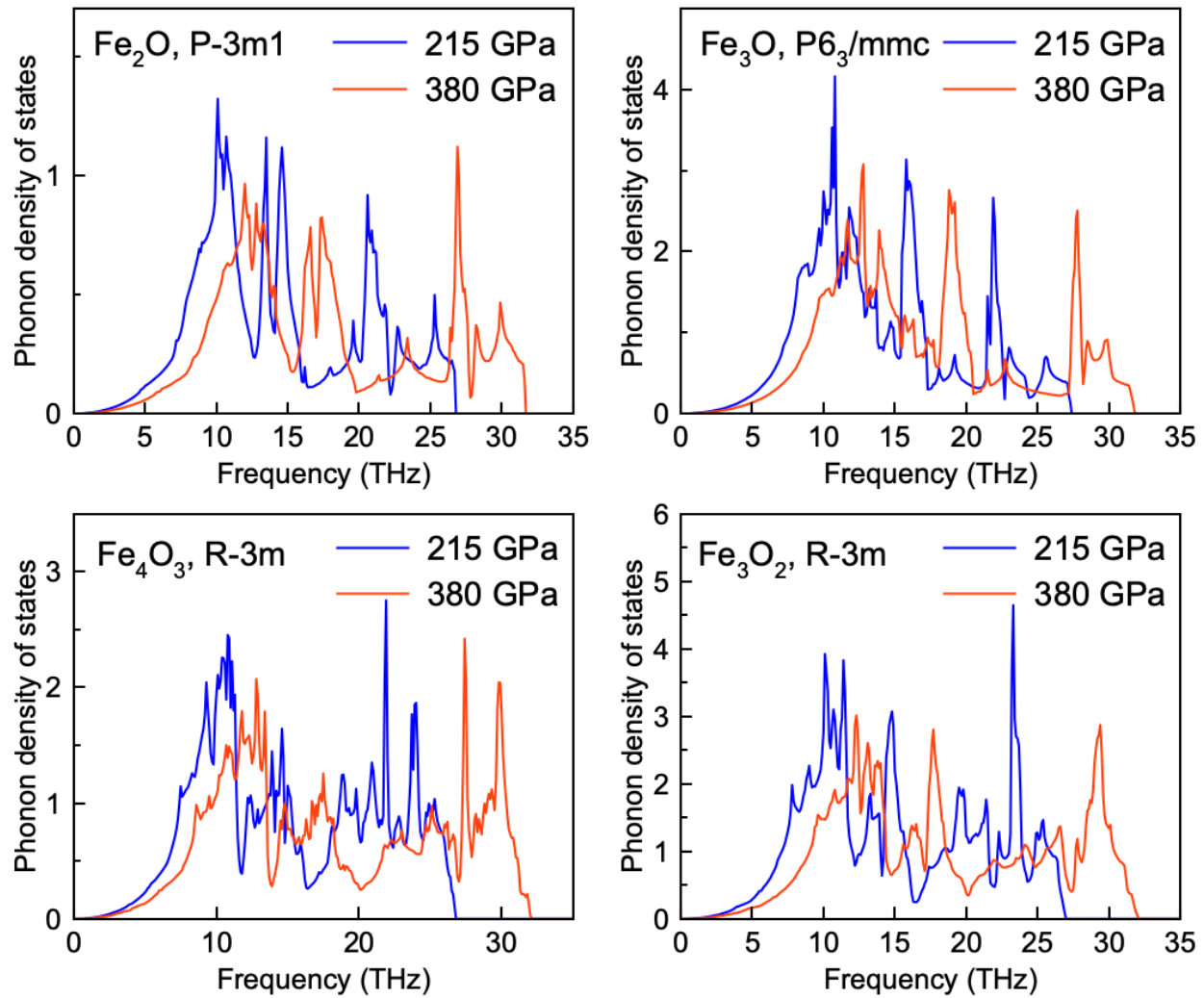


**Figure S9 | Phonon density of states of  $\text{Fe}_n\text{O}$  ground state.** The absence of imaginary phonon frequencies indicates that all phases are dynamically stable at 215 GPa and 380 GPa.

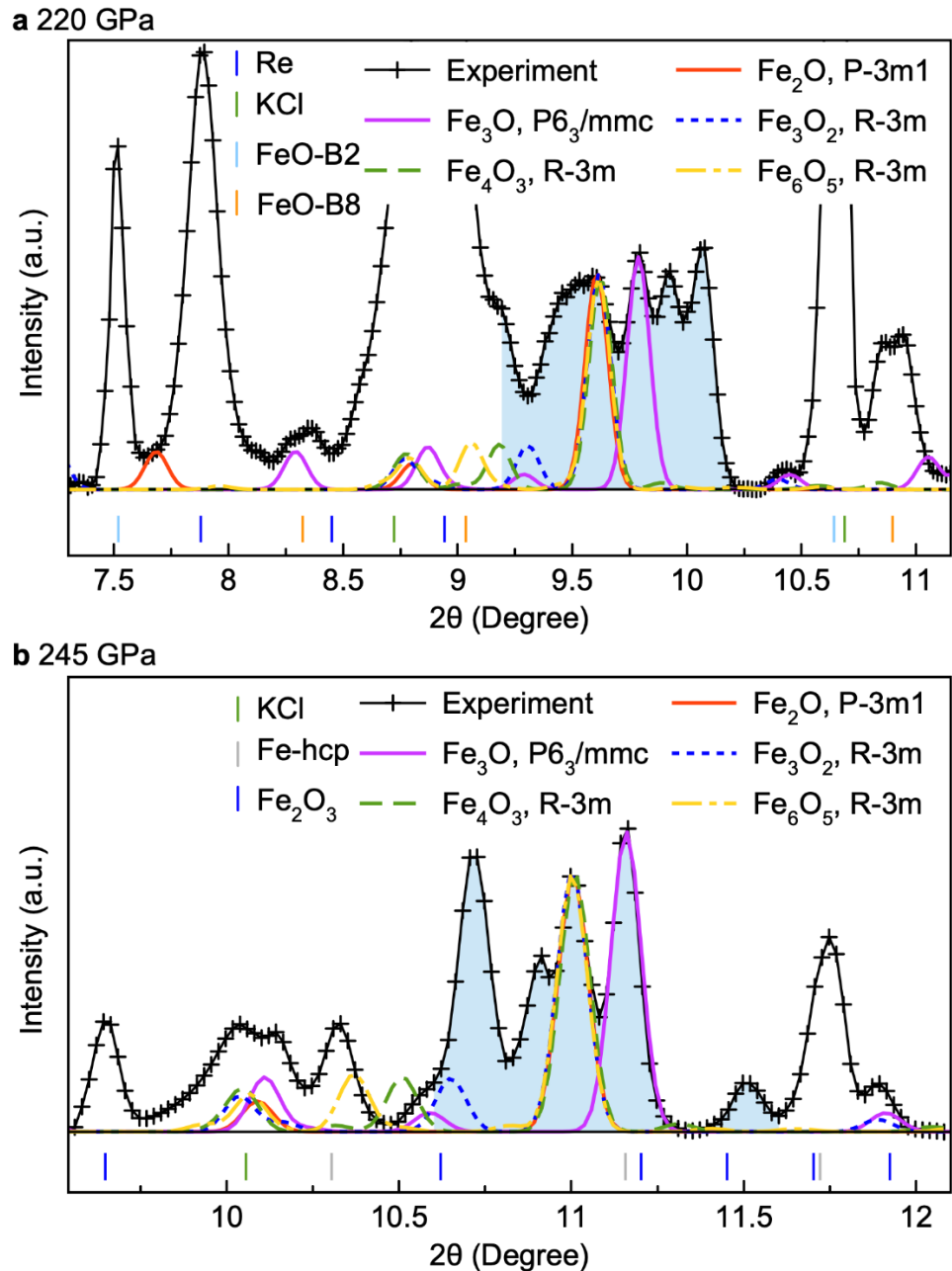


**Figure S10 | Comparison between experimental X-ray diffraction patterns and those of the  $\text{Fe}_n\text{O}$  phases in the convex hull found in the AGA searches.** The data were collected from (**a**)  $\text{Fe}+\text{FeO}$  reaction at 220 GPa and (**b**)  $\text{Fe}+\text{Fe}_2\text{O}_3$  reaction at 245 GPa. The XRD peak positions of starting materials are shown at the bottom.

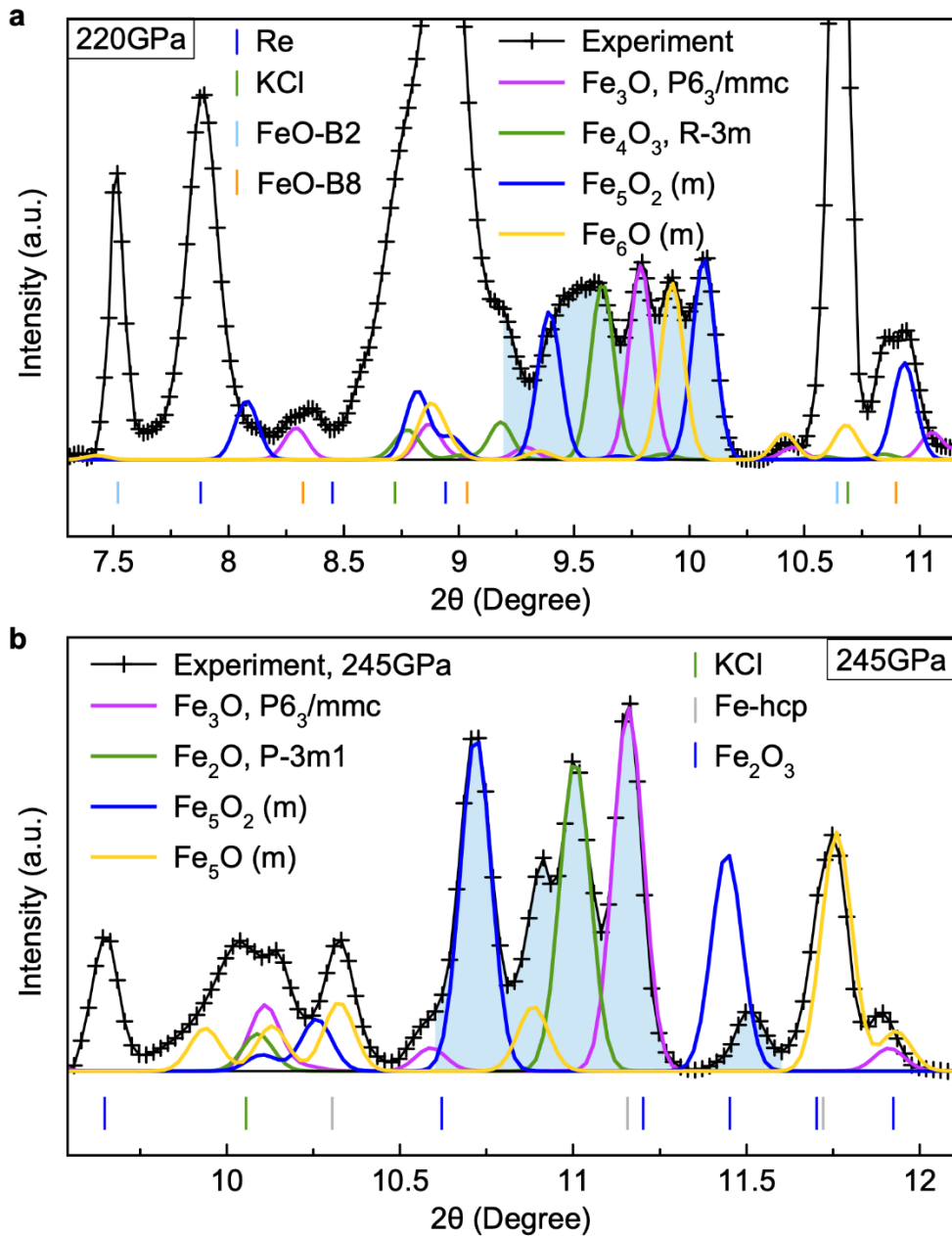


**Figure S11 | Multi-phase solution to the experimental XRD from (a) Fe+FeO reaction at 220 GPa and (b) Fe+Fe<sub>2</sub>O<sub>3</sub> reaction at 245 GPa.** The major unknown peaks in the experimental XRD can be matched by a combination of multiple close-packed Fe-O phases. (a)  $P6_3/mmc$  Fe<sub>3</sub>O and  $R-3m$  Fe<sub>4</sub>O<sub>3</sub> are ground state phases at 220 GPa while Fe<sub>5</sub>O<sub>2</sub> and Fe<sub>6</sub>O are metastable phases with 8.0 meV/atom and 4.5 meV/atom above the convex hull, respectively. (b) The same Fe<sub>3</sub>O and Fe<sub>2</sub>O phases are identified at 245 GPa, while Fe<sub>5</sub>O<sub>2</sub> and Fe<sub>5</sub>O are the metastable phases with 47 and 49 meV/atom above the convex hull, respectively.

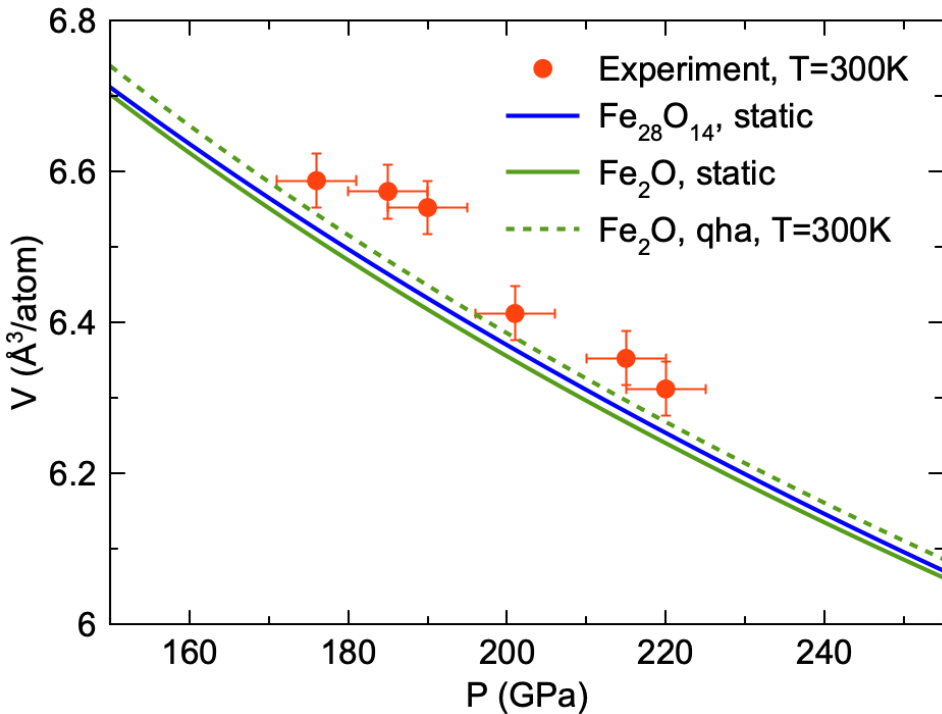


**Figure S12 | Experimental compression curve of products from Fe+FeO reaction and theoretical equation of state of the  $\text{Fe}_{28}\text{O}_{14}$  supercell (blue) and the  $\text{Fe}_2\text{O}$  ground state ( $P-3m1$ ) (olive).** Red symbols represent experimental data from the Fe-FeO reaction product upon decompression at room temperature. The decompression data is limited to  $\sim 170$  GPa because the x-ray diffraction signal of the new reaction product gradually faded away at pressures less than 200 GPa when the Fe-rich  $\text{Fe}_n\text{O}$  phase entered its unstable pressure field.

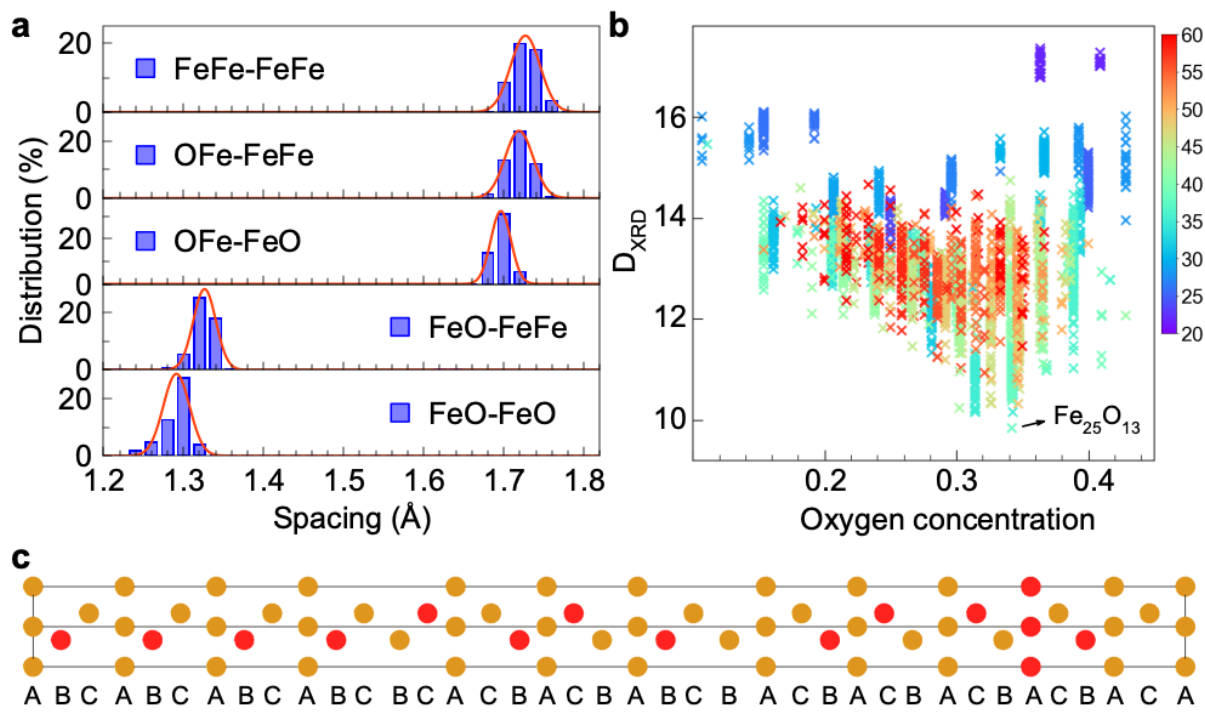


**Figure S13 | Reverse Monte Carlo solution for the XRD at 245GPa.** (a) Distribution of middle layer spacing in different layer sequences. The red curve is a fitting using a Gaussian distribution. (b) XRD deviation,  $D_{XRD}$ , vs. oxygen concentration for various hexagonal supercells resulting from various RMC simulations. Each point represents a final structure achieved by the simulation. Color indicates the number of atoms in the supercell. (c) Supercell structures of  $\text{Fe}_{25}\text{O}_{13}$ . The XRD of  $\text{Fe}_{25}\text{O}_{13}$  is shown in Fig. 1 of main text.

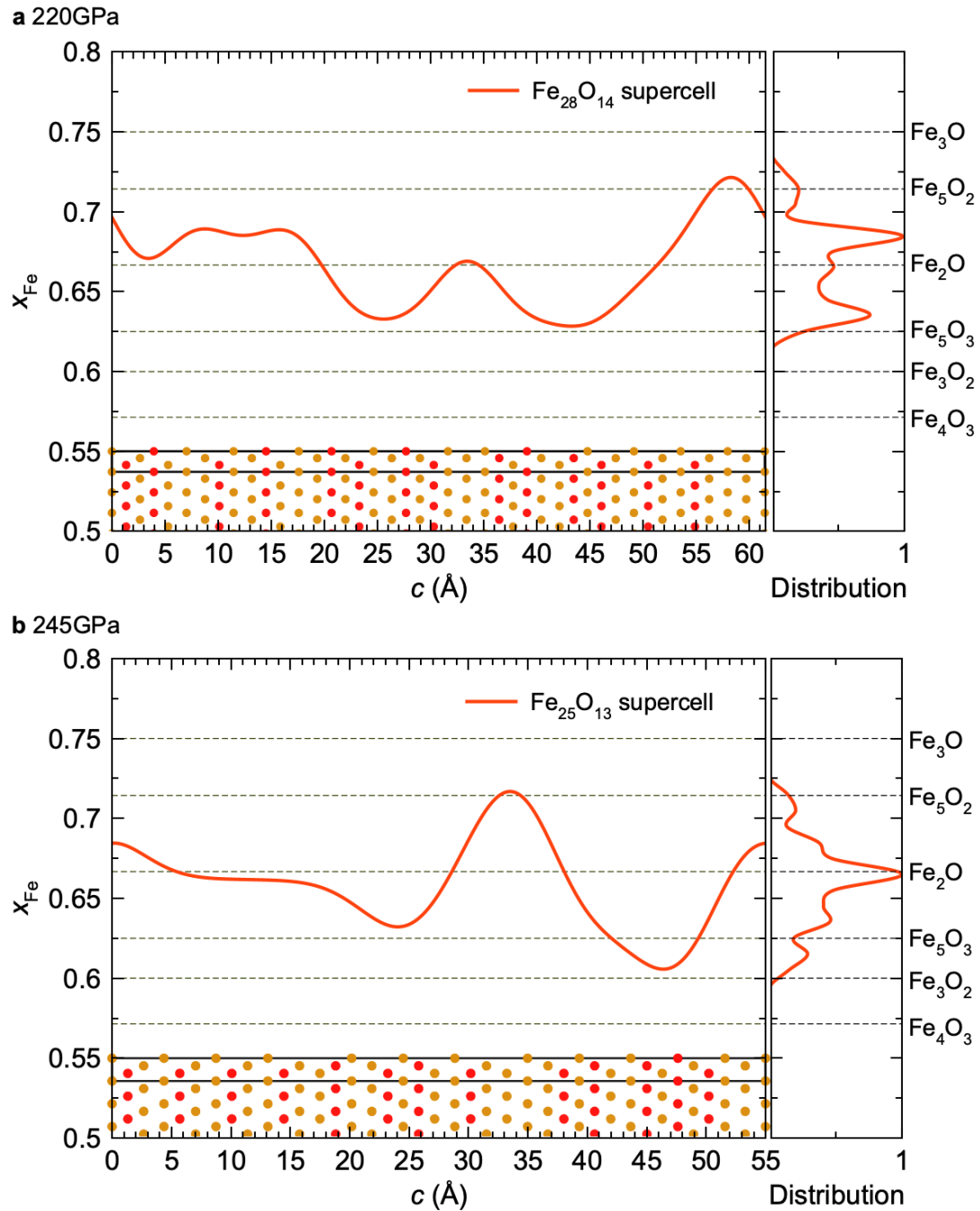


**Figure S14 | The profile of Fe composition ( $x_{\text{Fe}}$ ) along the out-of-layer  $c$ -axis direction.** (a) The  $\text{Fe}_{28}\text{O}_{14}$  supercell identified at 220 GPa and (b) The  $\text{Fe}_{25}\text{O}_{13}$  supercell identified at 245 GPa. The right panel is the distribution of the Fe local composition.

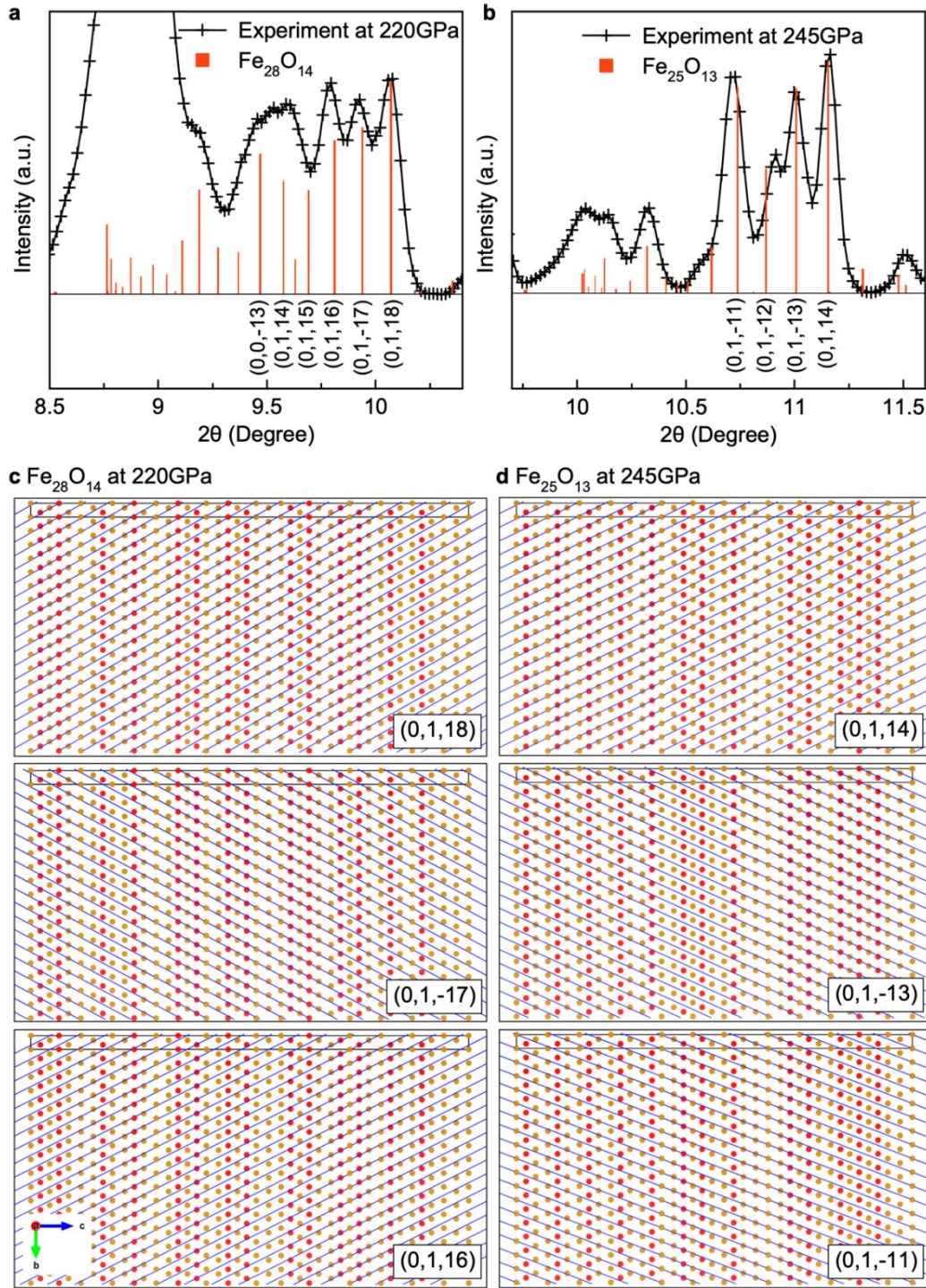


**Figure S15 | Miller indices and their corresponding lattice planes of major XRD peaks.** (a) and (b) Miller indices of major peaks and (c) and (d) corresponding lattice planes of supercell solutions obtained by RMC simulations at 220 GPa and 245 GPa, respectively.

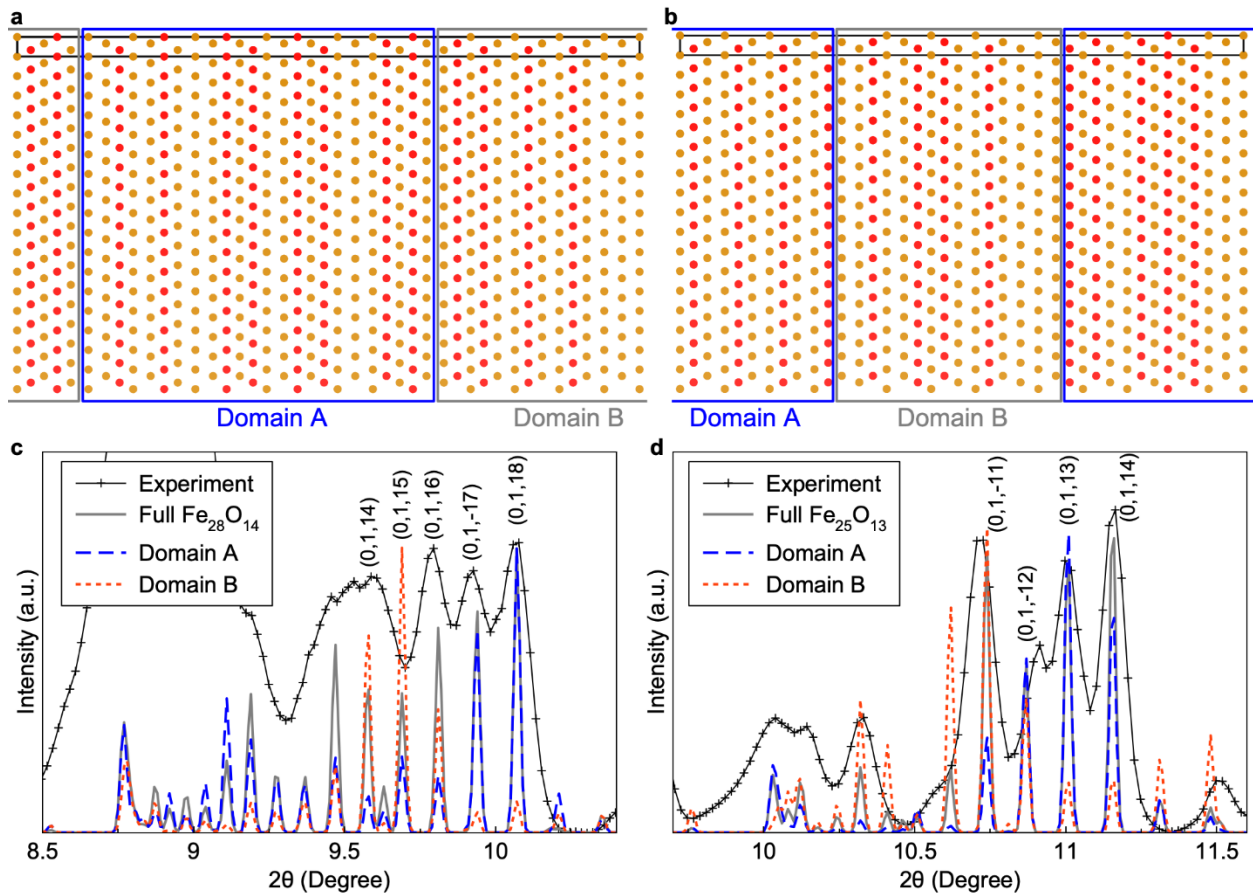


**Figure S16 | Domains with different MRO identified in the supercells and their contribution to the XRD.** (a) and (b) Domains in the Fe<sub>28</sub>O<sub>14</sub> and Fe<sub>25</sub>O<sub>13</sub> supercells. (c) and (d) The contribution of different domains to the XRD at 220 GPa and 245 GPa, respectively.

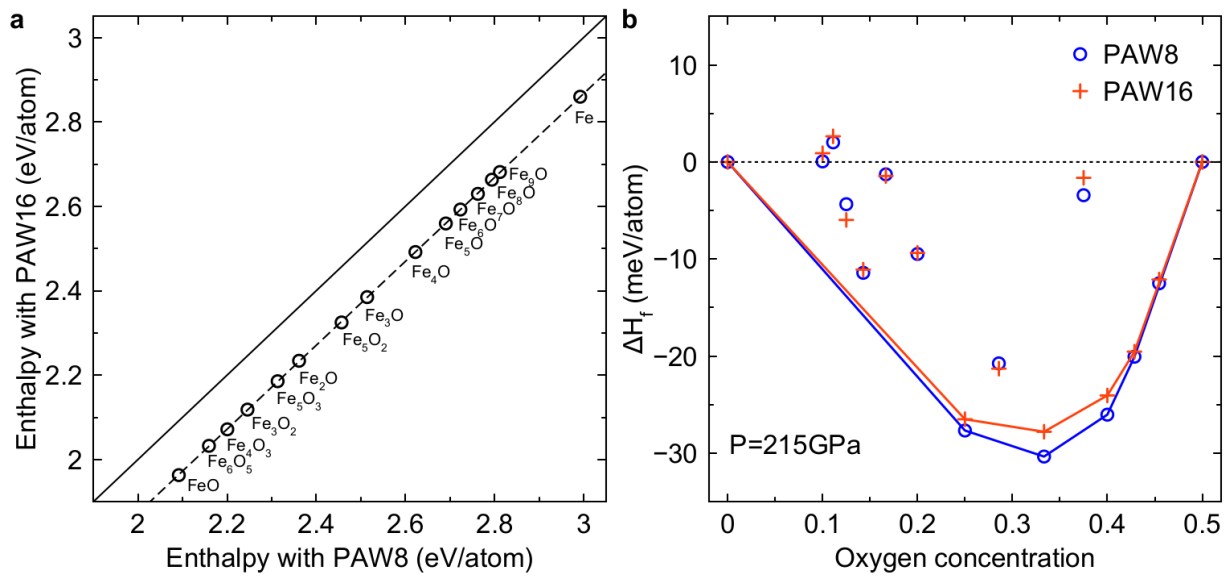


**Figure S17 | Comparison between PAW8 and PAW16 potentials.** **(a)** Scatter plot of enthalpies calculations with PAW8 and PAW16 potentials. The structures are the one with lowest enthalpy for each composition. **(b)** The formation enthalpy is computed using  $\epsilon$ -Fe and B8-FeO as reference. Phases in the convex hull are then connected.